Saracino et al. (2026)
The crystallization of Mercury's magma ocean and the formation of its primordial mantle structure
Advances in Geochemistry and Cosmochemistry 2(1): 1003, https://doi.org/10.33063/agc.v2i1.1003

Research article

The crystallization of Mercury's magma ocean and the formation of its primordial mantle structure

Fabrizio Saracino[1]✉ Bernard Charlier[1] Yishen Zhang[2,3] Olivier Namur[3]

[1] Department of Geology, University of Liege, 4000 Liege, Belgium
[2] Department of Earth, Environmental, and Planetary Sciences, Rice University, 6100 Main Street, MS 126, Houston, TX 77005, USA
[3] Department of Earth and Environmental Sciences, KU Leuven, Celestijnenlaan 200E, 3001 Leuven, Belgium

✉ **Correspondence to:** Fabrizio Saracino: f.saracino@uliege.be

Author contributions: Conceptualization: FS, BC, ON; Software: FS, BC, YZ, ON; Formal analysis: FS, ON; Investigation: FS; Data curation: FS; Writing — Original Draft: FS; Writing — Review & Editing: FS, BC, YZ, ON; Visualization: FS; Funding acquisition: FS, BC, ON; Supervision: BC.

Data, code, and outputs: Saracino et al. (2026): https://doi.org/10.5281/zenodo.20273496

Submitted: 2025-09-30
Accepted: 2026-05-01
Published: 2026-05-28

Production editor:
Ekaterina S. Kiseeva

Handling editor:
Raúl Fonseca

Reviews:
Nick Dygert
and one anonymous reviewer

Copyediting:
Yingbo Li,
Marthe Klöcking

Early in its history, Mercury underwent a magma ocean stage; its crystallization produced a primordial mantle and a flotation crust, setting the stage for early volcanism, crustal production, and thermochemical evolution. Here, we performed crystallization experiments on reduced, sulfur-rich silicate melt compositions relevant to Mercury's magma ocean and its solidification during cooling. Our approach aims to reconstruct the primordial mantle stratigraphy by combining a fractional crystallization model with phase equilibria experiments on a suite of residual melts at 1525–1125 °C and 1.5–0.5 GPa under low oxygen fugacity (-3.7 to -8.4 log units below iron-wüstite equilibrium) to investigate the crystallization sequence for two potential Bulk Silicate Mercury compositions: a low-Mg/Si melt in the enstatite stability field and a high-Mg/Si melt in the forsterite stability field. Residual melts become co-saturated in enstatite and forsterite, followed by the crystallization of clinopyroxene at melt fractions $F = 0.40$–0.35, quartz at $F = 0.28$–0.24, and plagioclase at $F = 0.19$–0.14. We define the evolution of the mantle cumulate pile and the thickness of the refractory and fertile reservoirs based on the appearance of clinopyroxene. We propose that Mercury's volcanic crust resulted from partial melting of the fertile mantle. Density calculations indicate that sulfur reduced the density of the silicate magma ocean, causing sulfides to become denser than the magma ocean, ultimately being stored in the mantle. We illustrate the influence of the magma ocean bulk composition ± sulfides on the storage and spatial distribution of heat-producing elements in Mercury's interior.

1 Introduction

Accretionary impacts, metal–silicate segregation, and the decay of short-lived radioisotopes would have produced enough thermal energy to completely melt Mercury during its very early evolution, forming a global silicate magma ocean (Schubert et al., 1988; Schaefer and Elkins-Tanton, 2018; Charlier and Namur, 2019). Subsequent crystallization of the magma ocean ultimately produced the primordial Mercurian mantle, whose vertical structure was determined by the crystallization regime and the initial composition of the bulk silicate Mercury (BSMe), although the latter remains debated (Brown and Elkins-Tanton, 2009; Nittler et al., 2018; Anzures et al., 2020; Mouser et al., 2021; Xu et al., 2024; Fischer and Parman, 2025). Experimental studies of surface lavas indicate significant compositional diversity within Mercury's mantle (Charlier et al., 2013; Namur et al., 2016a; Wang et al., 2022). Partial melting of certain chondritic precursors could also generate a wide variety of lava compositions, but this process alone cannot account for the full range of surface compositions observed on Mercury (Boujibar et al., 2025). Investigating the crystallization products of the Mercurian magma ocean (MMO) is thus crucial because its initial structure would have impacted convection and the thermal evolution of the mantle, setting the stage for mantle melt generation and effusive volcanism, which built the secondary crust until ~3.5 Ga (Brown and Elkins-Tanton, 2009; Byrne et al., 2016; McCoy et al., 2018; Boukaré et al., 2019; Mouser et al., 2021; Mouser and Dygert, 2023).

The MMO was unique among terrestrial planets: the MESSENGER spacecraft revealed the unusually high sulfur content and near FeO-free nature of Mercury's volcanic surface, which indicate highly reduced conditions (Nittler et al., 2011; McCubbin et al., 2012; Zolotov et al., 2013; Namur et al., 2016a). The high inferred bulk mantle S content (Namur et al., 2016a; Lark et al., 2022) has led authors to suggest that sulfide phases should have formed in the MMO, subsequently being stored in the mantle and/or primordial crust and potentially storing heat producing elements (HPEs; Boujibar et al., 2019; Boukaré et al., 2019; Pirotte et al., 2023). This process may have induced mantle overturn during post-magma ocean crystallization (Mouser and Dygert, 2023). Vander Kaaden and McCubbin (2015) suggested that graphite would have been the only buoyant phase in such a FeO–depleted MMO, the flotation of which likely contributed to the formation of a graphite primordial crust. Investigating melt density and the specific effect of sulfur in the cooling and evolving magma ocean is thus crucial to quantitatively evaluate if other light phases such as sulfides, quartz, and plagioclase could have become buoyant during solidification. Moreover, if containing significant amounts of HPEs, the distribution of sulfide phases could have substantially impacted Mercury's thermal evolution (Boujibar et al., 2019; Boukaré et al., 2019; Pirotte et al., 2023).

In this study, we present crystallization experiments aimed at reconstructing the vertical structure of Mercury's primordial mantle as a direct consequence of the fractional crystallization of the putative MMO. By combining these and previous experiments, we develop a phase equilibria-based crystallization model of the mineralogical and chemical evolution of the MMO from a range of BSMe compositions with different starting Mg/Si ratios. We further investigate the effect of sulfur content on the differentiation and density of the residual liquids, as well as the likelihood of crystalline phase flotation and its impact on the distribution of heat-producing elements. Our results refine our understanding of Mercury's early differentiation in terms of the mantle mineralogy under reduced conditions.

2 Bulk Silicate Mercury (BSMe)

Enstatite chondrites (ECs) have commonly been considered as analogs of Mercury's building blocks due to their similar geochemical features, including FeO–free silicate phases and high abundances of sulfur and alkali metals (Na, K; McCoy et al., 1999; Malavergne et al., 2010; Nittler et al., 2018; Fischer and Parman, 2025). The composition of the BSMe has been investigated by combining data from surface lavas with experiments simulating mantle melting (Namur et al., 2016a; Nittler et al., 2018) and by defining magmatic fractionation lines of surface and mantle compositions (Anzures et al., 2020; Fischer and Parman, 2025). Nittler et al. (2018) calculated the mantle source compositions of the high-Mg region and the North Volcanic Plains by considering the phase proportions and compositions of enstatite and forsterite reported by Namur et al. (2016a). Their results were similar to the silicate portion of enstatite chondrites and bencubbinites, adjusted to account for SiO_2 reduction to Si stored in the core under reduced conditions (e.g. Malavergne et al., 2010; Chabot et al., 2014). Recently, Fischer and Parman (2025) calculated a revised BSMe composition based on a new Mercury Fractionation Line (MFL) obtained by recalculating the Mg/Si and Al/Si ratios of X-Ray Spectrometer (XRS) data in McCoy et al. (2018). Because ECs are enriched in SiO_2 (Fig. 1), they calculated the amount of Si being reduced and removed to the core for each published EC composition until the Si-depleted compositions fell along the MFL. Anzures et al. (2020) proposed a modified CH3 chondrite composition (ALH 85085) as the best approximation of the BSMe, due to its similar Mg/Si, Al/Si, Fe/Si, and Ni/Si ratios.

The BSMe compositions considered in this study are inspired by the composition of the silicate fraction of enstatite chondrites (Fig. 1, Table 1; Xu et al., 2024; Saracino et al., 2025). An average composition was obtained from chemical analyses of both high-iron (EH) and low-iron (EL) enstatite chondrites (Jarosewich, 1990; Berthet et al., 2009). We also decreased the P_2O_5 content to account for the markedly siderophile behavior of P (Gu et al., 2019; Steenstra et al., 2020a; Pirotte et al., 2023). Some Si was also removed from the original chondritic composition: two compositions with different Mg/Si ratios were selected, corresponding to the segregation of 8 wt% and 15 wt% Si from the silicate fraction into the core (named Mer8 and Mer15, respectively; Xu et al., 2024; Saracino et al., 2025). Assuming that the core of Mercury represents 67 % of the planet's bulk mass (Hauck et al., 2013), these values reflect core Si contents of 2.9 wt% (Mer8) and 5.5 wt% Si (Mer15), spanning the lower range of estimated Si contents in the core of Mercury (Nittler et al., 2018). Our two compositions thus cover the BSMe compositional fields of Anzures et al. (2020) and Fischer and Parman (2025). Testing starting compositions with a range of different Mg/Si ratios is important because Mg/Si is known to promote the stability of enstatite or forsterite (Namur et al., 2016a; Anzures et al., 2020; Saracino et al., 2025).

3 Magma ocean modeling

3.1 Fractional crystallization modeling

We follow the modeling strategy of Elkins-Tanton et al. (2003) and Charlier et al. (2018), who developed a numerical code to simulate the crystallization of the Martian and lunar magma oceans, respectively. Our code (Saracino et al., 2026) is rooted in experimentally determined phase equilibria and traces the solidification steps of the MMO through a stepwise approach in which we calculate the mineralogy, composition, and density of cumulates while tracking the compositional evolution of the residual silicate liquids. The initial compositions of the silicate liquid are the primitive compositions Mer8 and Mer15. Major elements and heat-producing elements (U, Th, K) were considered. FeO was excluded from the input compositions because MESSEN-

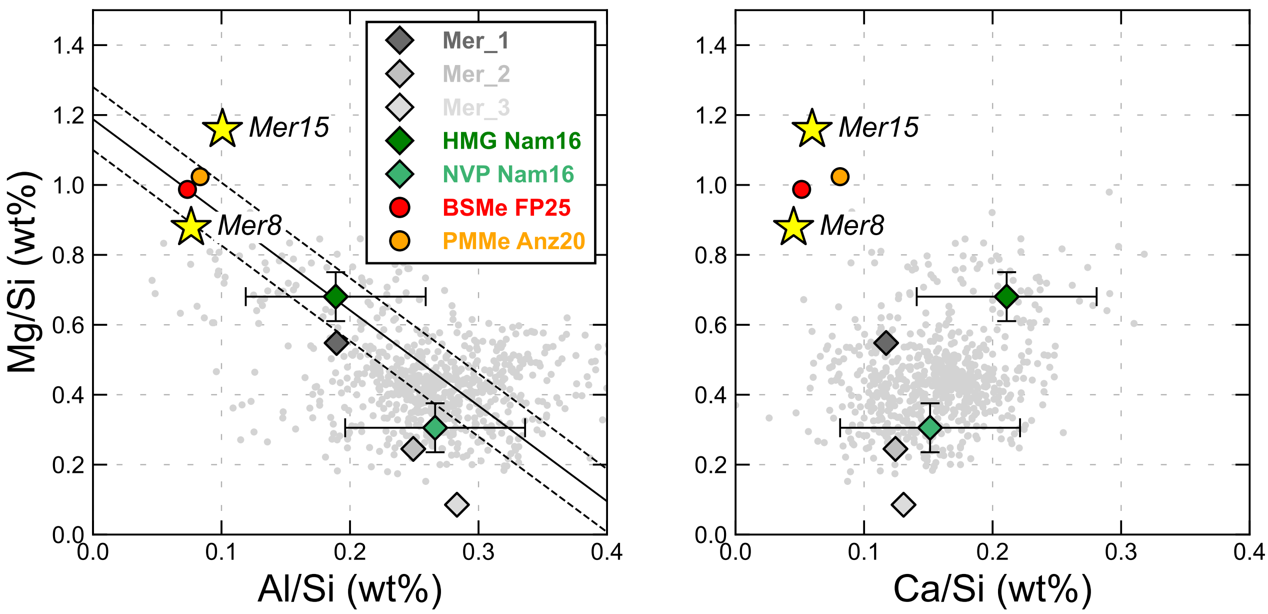

Figure 1. Elemental ratios of major elements (wt%) of our starting compositions for (a) Al/Si versus Mg/Si and (b) Ca/Si versus Mg/Si. Also shown for comparison are the Bulk Silicate Mercury (BSMe) from Fischer and Parman (2025), the Primitive Mantle of Mercury (PMMe) from Anzures et al. (2020), and the Northern Volcanic Plains (NVP) and the High-Mg Intercrater Plains (HMG) from Namur et al. (2016b). Small grey circles are XRS measurements from Weider et al. (2015). The black solid line in (a) is the Mercury Fractionation Line (MFL), with relative upper and lower bounds (dashed lines) as calculated in Fischer and Parman (2025).

GER data have demonstrated the paucity of FeO on the surface (Nittler et al., 2020). Fractional crystallization is described as (Namur et al., 2012; Charlier et al., 2018; Zhang et al., 2024):

$$c^0_{i,Liq} = (1-z)c^1_{i,Liq} + z\left[\left(\sum_{j=1\rightarrow n} X^j c^j_i\right) X^{Mush}_{Sol} + c^0_{i,Liq} X^{Mush}_{Liq}\right] \tag{1}$$

where z is the crystallization increment (fixed at 1 % of the residual liquid; i.e. z becomes increasingly small as crystallization proceeds), $c^1_{i,Liq}$is the concentration of element i, bonded to oxygen, in the liquid at each step of fractionation, $c^0_{i,Liq}$ is that during the previous step of fractionation, c^j_i is the concentration of element i in solid phase j, X^j is the proportion of phase j in the cumulate assemblage, and X^{Mush}_{Sol} and X^{Mush}_{Liq} are the bulk proportions of the solid phases and trapped liquid in the solidifying crystal mush.

To determine the density of the silicate liquid produced during MMO crystallization, we first calculated the density at zero pressure as:

$$\rho_{Liq} = \sum \frac{Q_i M_i}{Q_i V_i} \tag{2}$$

where Q_i is the molar fraction of component i in the melt, M_i is its molar mass, and V_i is its partial molar volume. Density is then adjusted to account for the effect of pressure and temperature with a third order Birch-Murnaghan equation of state:

$$P = \frac{3}{2}k_T\left[\left(\frac{V_0}{V_f}\right)^{\frac{7}{3}} - \left(\frac{V_0}{V_f}\right)^{\frac{5}{3}}\right] \cdot \left\{1 - \left(\frac{3}{4}\right)(4-k'_T)\left[\left(\frac{V_0}{V_f}\right)^{\frac{2}{3}} - 1\right]\right\} \tag{3}$$

where P is pressure, k_T is Young's modulus, V_0 is the initial molar volume, V_f is the molar volume at pressure P, and k'_T is the pressure derivative of k_T. k_T and k'_T were determined via multiple linear regression of literature data as a function of major element melt compositions (Ohtani and Maeda, 2001; Guillot and Sator, 2007). The temperature dependence of the liquid density is calculated using the compositional expression of thermal expansion from Lange and Carmichael (1987). The parameters used to calculate the melt density are reported in the Supplementary Material (Section S.1). Other equations of state used for the calculation of the liquid density are shown for comparison in Figure S1 (in the Supplementary Material). The effect of S on the density of the silicate liquid is poorly constrained in the literature, and a specific discussion of this aspect is presented in Section 6.4.

Magma oceans are considered to crystallize from the bottom up and to strongly convect, such that no chemical gradient is assumed (Walker et al., 1975; Brown and Elkins-Tanton, 2009). Starting from the density of the cumulus phases, the thickness of the different layers can be calculated as crystallization proceeds at each increment z.

Table 1. Compositions of starting materials (expressed in wt%). Also shown are (a) pre-melting mantle compositions of the Northern Smooth Plains and Intercrater Highly cratered Terrains (Nittler et al., 2018); (b) PMM, the Primitive Mercurian Mantle (Anzures et al., 2020), (c) Bulk Silicate Mercury (Fischer and Parman, 2025), and (d) Bulk Silicate Earth (McDonough, 2025). Abbreviations: n.d., not determined.

	Primitive compositions		Pre-melting mantle (NSP)[a]	Pre-melting mantle (IcP HCT)[a]	Primitive Mantle Mercury[b]	Bulk Silicate Mercury[c]	Bulk Silicate Earth[d]
	Mer8	Mer15					
SiO_2	54.82	47.91	53.67	51.98	51.32	52.06	44.92
TiO_2	0.14	0.16	0.24	0.21	0.21	0.13	0.20
Al_2O_3	3.70	4.26	4.57	4.24	3.78	3.38	4.19
Cr_2O_3	0.52	0.60	n.d.	n.d.	0.41	0.54	0.33
FeO_{tot}	n.d.	n.d.	0.02	0.03	0.54	0.20	8.05
MnO	0.28	0.33	n.d.	n.d.	0.09	0.31	0.14
MgO	37.32	43.04	36.89	37.64	40.72	39.84	37.81
CaO	1.62	1.87	2.26	3.84	2.73	1.75	3.27
Na_2O	1.37	1.58	1.97	1.29	0.08	1.62	0.36
K_2O	0.13	0.15	0.05	0.04	0.02	0.17	0.03
P_2O_5	0.10	0.10	n.d.	n.d.	n.d.	n.d	0.02
NiO	n.d.	n.d.	n.d.	n.d.	0.11	n.d	0.22
Total	100.00	100.00	99.67	99.27	100.01	100.00	99.54
Mg/Si	0.88	1.16	0.89	0.93	1.02	0.99	1.09
Ca/Al	1.18	1.18	1.34	2.45	1.95	1.40	2.11

3.2 Depth of the magma ocean

The initial depth of the MMO was calculated using gravity models for Mercury. A smaller polar moment of inertia (MOI; 0.333 ± 0.005; Genova et al., 2019) yields a deeper core-mantle boundary (CMB), and therefore a deeper interface between the magma ocean and the metallic core ($\sim 485 \pm 20$ km depth in Goossens et al., 2022; ~ 463 km in Steinbrügge et al., 2021). Conversely, models with a higher MOI (0.346 ± 0.014; Margot et al., 2012) return a shallower CMB interface at ~ 430 km depth (Bertone et al., 2021). In this work, we simulate the crystallization of the MMO from an initial depth of 480 km, corresponding to the maximum possible CMB depth. Accordingly, we account for a higher volume of the silicate magma ocean, which is considered to have been ~ 17 % greater than the present-day solid silicate shell.

3.3 Early crystallization stages

Literature data on near-liquidus experiments representative of the BSMe provide precious insights into the phase equilibria of early forming minerals (Anzures et al., 2020; Xu et al., 2024; Saracino et al., 2025). Xu et al. (2024) and Saracino et al. (2025) showed that enstatite is the liquidus phase in sulfide-saturated Mer8 (Mg/Si = 0.88) whereas forsterite is the liquidus phase in sulfide-saturated Mer15 (Mg/Si = 1.16) between 1 and 7 GPa. Interestingly, Saracino et al. (2025) showed that the residual melt compositions of sulfide-saturated Mer8 and Mer15 converge, eventually reaching a single cotectic curve after sufficient differentiation. The initial fractionation of the MMO can therefore be simulated by fractionating only enstatite for Mer8 and only forsterite for Mer15 until the residual MMO liquids reach the forsterite-enstatite cotectic (Fig. 2). After reaching this cotectic curve, all Mercurian melts, including low- and high-Mg/Si melts, evolve towards the same eutectic where crystallization ends (Namur and Charlier, 2017). Accordingly, during the first stage of crystallization, the Mg/Si ratios of the Mer8 and Mer15 residual liquids converge until they cross at ~ 2.6 GPa (Fig. 3). To further evolve the MMO, we consider an average of the two residual liquid compositions (Fig. 3).

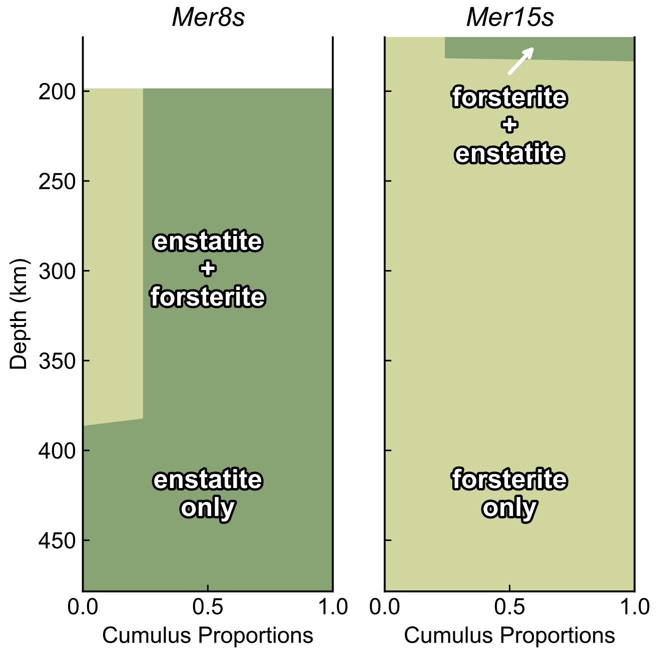

Figure 2. The early crystallization sequence for S-bearing Mer8 and Mer15 compositions. Light green refers to forsterite; dark green refers to enstatite.

The second stage of the forward model is the co-crystallization of forsterite and enstatite. The

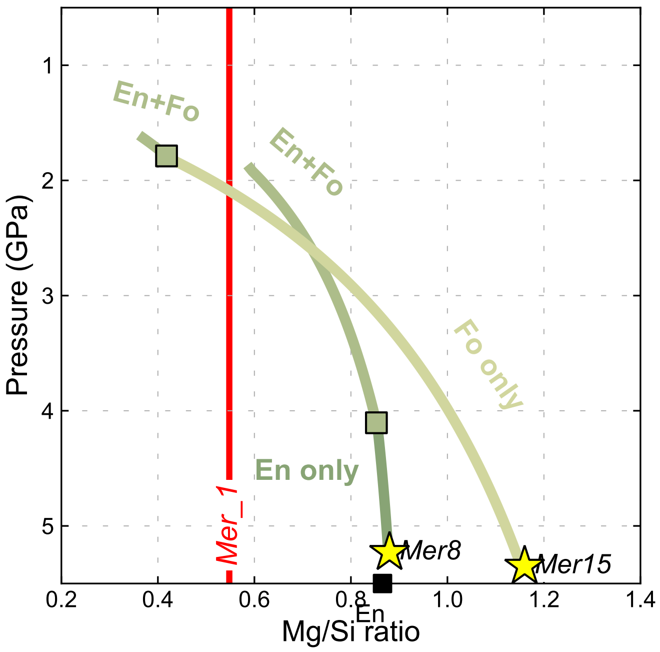

Figure 3. Mg/Si ratio as a function of pressure (GPa) in the early crystallization sequence for both Mer8 and Mer15 compositions. The red line refers to the Mg/Si ratio of Mer_1, which corresponds to the cotectic composition at which forsterite and enstatite coexist (see Section 4.1 for details). The black square corresponds to the composition of enstatite (En).

instantaneous relative proportions of forsterite and enstatite in the cumulate assemblage can be obtained from the tangent to the cotectic curve. We thus plotted experimental melts saturated with both forsterite and enstatite relevant to Mercury's mantle compositions (Xu et al., 2024; Saracino et al., 2025) in the diopside-SiO_2-forsterite ternary system (Fig. S2 in Section S.2). The plotted melts were produced from the same starting materials (Mer8 and Mer15) over a wide pressure range (1.5–7.0 GPa). Calculated mineral proportions from these experimental melts returned a range of relative proportions, from around $Fo_{42}En_{58}$ to $Fo_{10}En_{90}$, with higher pressures producing a higher Fo/En ratio due to the expansion of the enstatite stability field relative to that of forsterite with increasing pressure (Bowen, 1914; Kushiro, 1969; Chen and Presnall, 1975; Falloon and Green, 1988; Weng and Presnall, 2001, Fig. S2). As an approximation, we therefore considered a rough average of the relative proportions: $Fo_{25}En_{75}$.

4 Experimental and analytical methods

4.1 Experimental strategy

Our experimental study aims to simulate the evolution of the silicate liquid in the MMO during cooling and with decreasing pressure as the cumulate pile thickens while the melt fraction (F) decreases. We used a stepwise approach to simulate the fractional crystallization of the BSMe. Starting composition Mer_1 corresponds to the cotectic composition at which forsterite and enstatite coexist, following the crystallization of forsterite from Mer15 and enstatite from Mer8 using the forward crystallization model described above (Fig. 3). Experiments were performed with the Mer_1 composition until clinopyroxene joined the mineral assemblage with forsterite and enstatite. We then used the new residual melt composition in equilibrium with clinopyroxene, Mer_2, in further experiments until the appearance of quartz, which also corresponded to the destabilization of forsterite due to the high activity of SiO_2 (a_{SiO_2}). Lastly, a final composition produced from the Mer_2 residual melts, Mer_3, was used to reach the most evolved stages of magma ocean solidification. These three starting compositions are reported in Table 2. Each new series of experiments pertaining to new starting materials were performed at progressively lower pressure-temperature conditions to simulate the incipient cooling and thinning of the residual MMO. The P-T-F profile and the complete crystallization sequence were obtained by combining the experimental results and the forward crystallization model. In total, our experiments span temperatures of 1525–1125 °C and pressures of 1.5–0.5 GPa (Fig. 4).

4.2 Starting materials

The starting materials (Table 2) were produced from high-purity oxide powders: SiO_2, TiO_2, Al_2O_3, Cr_2O_3, MnO, MgO, $CaSiO_3$, Na_2SiO_3, $K_2Si_4O_9$, and $AlPO_4$. $CaSiO_3$, Na_2SiO_3, and $K_2Si_4O_9$ were produced by decarbonating mixtures of carbonates and SiO_2. Sulfur was added as FeS, FeS + S, or only as elemental S powder. Powders were mixed in an agate mortar with methanol and then stored in an oven at 120 °C. Different oxygen fugacity (fO_2) conditions were achieved by using different metallic Si/SiO_2 molar ratios in the starting materials: 0, 0.10, 0.20 (referred to as Mer(0), Mer(10), Mer(20)). Although fO_2 may not affect the stability of silicate phases in the Fe-free system, it affects S solubility in the melt and therefore the timing and nature of sulfide saturation (Namur et al., 2016b). With this approach, we were able to track the range of sulfides that can be produced using different Fe/S ratios. Neither S nor Si were added to Mer_3(0) because the solubility of S was observed to be low (< 0.5 wt% S) in Mer_2 at temperatures below 1250 °C, in accordance with the decreasing solubility of S with decreasing T and increasing SiO_2 content (Namur et al., 2016b).

4.3 Experimental methods

Experiments were conducted with a Voggenreiter Mavo LPC 250-300/50 end-loaded piston-cylinder apparatus at the University of Liège (Belgium). Half inch (1/2") assemblies were used in the pressure range 1.0–1.5 GPa, and 3/4" assemblies for runs at 0.5 GPa. For the 1/2" assembly, a graphite capsule with a MgO spacer was placed in a graphite furnace, and a $BaCO_3$ cell was used as the pressure medium. In the 3/4" assembly, a talc + pyrex cylinder was used as the pressure medium. Details on the cell assemblies employed in this study are reported in the Supplementary Material (Fig. S3). Temperature was monitored with a $W_{75}R_{25}/W_{97}R_3$ D-type thermocouple for both assemblies.

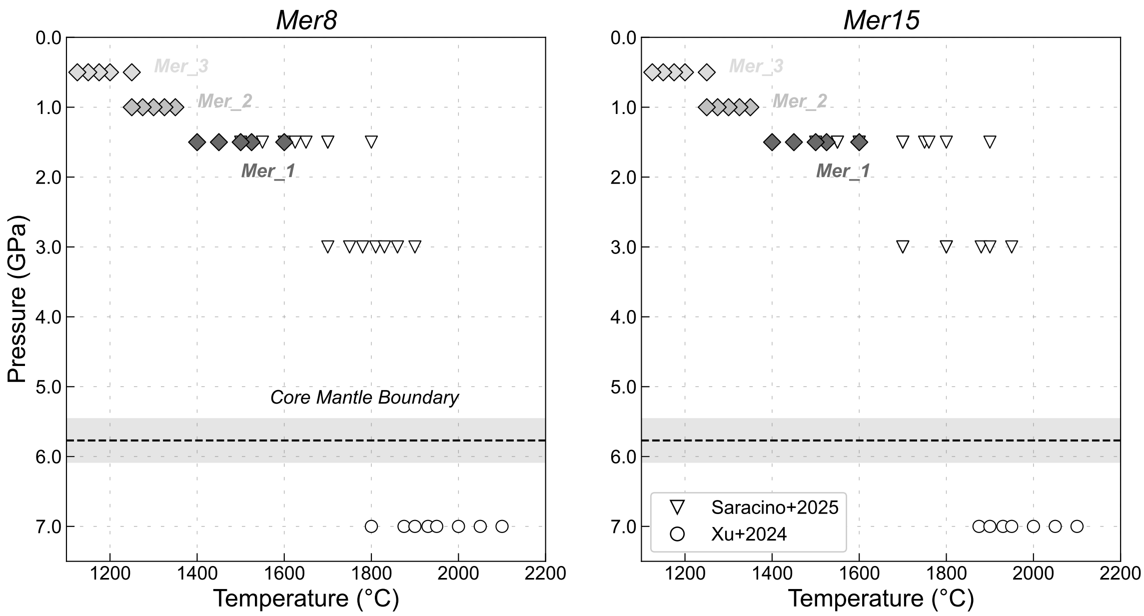

Figure 4. Pressure and temperature conditions of our experimental runs representing the evolution of the residual MMO liquid. Experiments are from this study (diamonds with various shades of grey), Saracino et al. (2025, white downward inverted triangles), and Xu et al. (2024, white circles). The pressure estimate at the core-mantle boundary and relative upper and lower bounds are from Xu et al. (2024).

A correction was applied for the temperature gradient between the tip of the thermocouple and the center of the capsule, which we estimate to be ∼25 °C. The assemblies were first pressurized at room temperature to 0.7 GPa in the 1/2" setup and 0.4 GPa in the 3/4" setup. Then, temperature was increased to 865 °C at 100 °C/min while keeping the pressure constant. Temperature was then held for 6 min to pressurize to the target pressure. Finally, temperature was increased again at 50 °C/min until the target temperature was attained. Friction correction coefficients of 9.3 % for the 1/2" assembly and 20 % for the 3/4" assembly were applied, respectively (Condamine et al., 2022). Experiments were quenched by switching off the power. Experimental samples were cut in half using a diamond wafer saw, mounted in epoxy, and ultimately polished with an alcohol-based polycrystalline 1 µm diamond suspension preserving all sulfides.

4.4 Attainment of equilibrium

We performed time-series experiments to test the attainment of equilibrium and the potential loss of volatiles through the graphite capsule (Na, S). Four experiments at 1300 °C and 1 GPa were run at different durations (30 min, 1 h, 3 h, 6 h) using Mer_2(20) as the starting material. In all of these samples, enstatite, clinopyroxene, and quartz coexisted with the silicate melt, and these three crystalline phases produced small euhedral crystals regardless of the duration investigated. As commonly observed in experiments with Si/$SiO_2 = 0.20$, a slight excess of Si metal (∼1 wt%) was observed in all four experiments. The compositions of the silicate glasses (Fig. S4 in the Supplementary Material; Saracino et al., 2026) show that sulfur was readily incorporated into the melt after 30 min and slightly decreased after one hour (from 3.4 to 2.7 wt%; Fig. S4d). No substantial loss of Na was observed at durations up to 6 h (Fig. S4c). We also observed that the concentration of Si in the silicate glass slightly increased at durations longer than 1 h (Fig. S4a), explained by the likely oxidation of residual Si metal in longer duration runs. The progressive oxidation of the system is corroborated by the slight depletion of Si in the metallic phase (Fig. S5) over durations longer than 1 h and the lower solubility of S in the silicate melt in longer experiments. Based on these results, we conclude that we approached thermodynamic equilibrium within ∼1 h.

4.5 Analytical methods

Imaging and phase identification were performed with the TESCAN MIRA 4th Generation Scanning Electron Microscope (SEM) at the Department of Geology, KU Leuven (Belgium). Quantitative analyses of our experimental products were conducted with the JEOL JXA-8530F electron probe micro-analyser (EPMA) at the Department of Materials Engineering, KU Leuven. Silicate crystals and sulfide and metallic phases were measured with a 15 kV accelerating voltage and 10 nA beam current. Silicate melts (glass) were measured with a 15 kV accelerating voltage and a 15 nA beam current. Crystals were analyzed with a focused beam and glasses with a beam defocused to 5–20 µm depending on the size of the glass pool. Sulfides were measured with a focused beam and metals with either a focused or a defocused beam (5–10 µm) depending on the size of the metallic phase and the presence of heterogeneities and quench textures. Peak counting times were 10–30 s and

Table 2. Residual liquid compositions (Series 1–3) compared to the starting chondritic compositions Mer8 and Mer15 (Series 0). n.d., not determined.

	Series 0		Series 1				Series 2		Series 3
	Mer8	Mer15	Mer_1	Mer_1 FeS	Mer_1 FeS, S	Mer_1 S	Mer_2	Mer_2 FeS	Mer_3
SiO_2	54.82	47.91	56.53	45.22	45.22	48.05	62.91	52.22	66.48
TiO_2	0.14	0.16	0.38	0.30	0.30	0.32	0.17	0.14	0.16
Al_2O_3	3.70	4.26	9.46	7.57	7.57	8.04	13.85	11.50	16.62
Cr_2O_3	0.52	0.60	0.56	0.45	0.45	0.48	0.11	0.09	0.02
MnO	0.28	0.33	0.37	0.30	0.30	0.31	0.31	0.26	0.04
MgO	37.32	43.04	24.01	19.21	19.21	20.41	11.95	9.92	4.39
CaO	1.62	1.87	4.33	3.46	3.46	3.68	5.12	4.25	5.68
Na_2O	1.37	1.58	3.75	3.00	3.00	3.19	5.10	4.23	6.00
K_2O	0.13	0.15	0.36	0.29	0.29	0.31	0.49	0.41	0.60
P_2O_5	0.10	0.10	0.26	0.21	0.21	0.22	n.d.	n.d.	n.d.
FeS				20.00	10.00			17.00	
S					10.00	15.00			
Total	100.00	100.00	100.00	100.00	100.00	100.00	100.00	100.00	100.00

background counting times on each side of the peak were 5–15 s for each element. We employed both natural and synthetic standards. For silicate crystals we used albite for Na, orthoclase for K and Al, diopside for Ca, olivine for Si and Mg, rutile for Ti, MnO for Mn, Cr_2O_3 for Cr, and fayalite for Fe. For silicate glass we used albite for Na, obsidian for K and Al, olivine for Mg, diopside for Ca, rutile for Ti, rhodonite for Mn, Cr_2O_3 for Cr, hematite for Fe, and $BaSO_4$ for S. For sulfide and metallic phases we used albite for Na, Si metal for Si, diopside for Ca, olivine for Mg, obsidian for Al, rutile for Ti, Cr metal for Cr, Fe metal for Fe, Mn metal for Mn, and pyrite for S. Replicate measurements of international standards indicate analytical errors of less than 5 % for major elements and 10–15 % for minor elements. For sulfur measurements in the silicate glass, reliability was attained through accurate calibration and reproducibility on $BaSO_4$, which suggest errors below 10–15 %. Raw data were corrected for matrix effects with the CATZAF software.

4.6 Determination of Oxygen fugacity

Under reduced conditions, the oxygen fugacity of the experimental charges can be calculated considering the equilibrium between Fe metal and FeO-bearing silicate melts as (Corgne et al., 2008):

$$Fe_{Metal} + \frac{1}{2}O_2 \ = \ FeO_{Melt} \tag{4}$$

The activity of Fe in the metal a_{Fe} is given by:

$$a_{Fe} = Q_{Fe}\gamma_{Fe} \tag{5}$$

where Q_{Fe} is the molar content of Fe in the Fe metal and γ_{Fe} is the activity coefficient of Fe. Analogously, the activity of FeO in the silicate melt a_{FeO} is given by:

$$a_{FeO} = Q_{FeO}\gamma_{FeO} \tag{6}$$

where Q_{FeO} is the molar content of FeO in the silicate melt and γ_{FeO} is the activity coefficient of FeO. However, typical Mercurian melt compositions have extremely low FeO contents (< 1 wt%) and are close to or below the detection limit of analytical instruments. Measurements uncertainties for low FeO concentrations may therefore limit the accuracy of fO_2 estimates (Cartier et al., 2014; Namur et al., 2016a; Anzures et al., 2020; Steenstra et al., 2020a; Pirotte et al., 2023). Nonetheless, under FeO-poor conditions, fO_2 can be determined using the equilibrium between Si-rich metal and SiO_2 in the silicate melt as (Cartier et al., 2014):

$$SiO_{2,\ Melt} = Si_{Metal} + \ O_2 \tag{7}$$

where $SiO_{2,\ Melt}$ is the SiO_2 concentration in the melt and Si_{Metal} is the Si concentration in the metal. The activity of Si in the metal is given by:

$$a_{Si} = Q_{Si}\gamma_{Si} \tag{8}$$

with Q_{Si} being the molar Si content in the metal and γ_{Si} the activity coefficient of Si. Here we use the Si activity coefficients calculated following Ma (2001). Similarly, the activity of SiO_2 in the silicate melt is calculated as:

$$a_{SiO_2} = Q_{SiO_2}\gamma_{SiO_2} \tag{9}$$

where Q_{SiO_2} is the molar SiO_2 content in the melt and γ_{SiO_2} is the activity coefficient of SiO_2. For experiments that do not saturate silica phases (A399, A397, A396, A404), a_{SiO_2} was calculated based on the reaction $Mg_2SiO_4 + SiO_2 = Mg_2Si_2O_6$ (Saracino et al., 2025). In experiments that saturate silica phases, a_{SiO_2} can be approximated as ∼ 1 (Cartier et al., 2014). Only for runs in which no Si-bearing Fe metal was available (A461, A462, A469) did we calculate oxygen fugacity following the method of Namur et al. (2016b), where the oxygen fugacity can be calculated based on the sulfur content at sulfide saturation (SCSS) as:

$$\ln[S]_{SCSS} = a + \frac{b}{T} + \frac{cP}{T} + d\log(fO_2) + \sum e_i\frac{X_i}{X_{SiO_2}} \tag{10}$$

where $[S]_{SCSS}$ is the SCSS (in wt%), T is temperature (in K), P is pressure (in bar), fO_2 is the oxygen fugacity, X_i are the molar fractions of oxides in the silicate melt (renormalized to 100 % on a S-free basis), and a, b, c, d, $e\text{TiO}_2$, $e\text{MgO}$, and $e\text{Na}_2\text{O}$ are derived coefficients.

The fO_2 in experiments containing Si-bearing Fe metal spans the range from IW-5.8 to IW-8.4. The coexistence of excess Si metal and quartz suggests that some experiments are buffered at Si–SiO_2 equilibrium. For experiments that did not contain Si-bearing metal, we calculated the oxygen fugacity to be between IW-3.7 and IW-3.9.

5 Results

5.1 Experimental textures and phase equilibria

Representative backscattered electron images of the experimental products are shown in Figure 5. All experimental runs, P-T-fO_2 conditions, and phase assemblages are reported in Table 3. Mer_1 contained enstatite as the liquidus mineral at $T = 1500\,°\text{C}$, so slightly offsets from the predicted enstatite-forsterite cotectic. Forsterite and clinopyroxene then appeared at $T = 1450\,°\text{C}$. Enstatite and forsterite occurred as relatively large (5–50 µm) euhedral crystals (Fig. 5a), and clinopyroxene as small (< 10 µm), bright crystals often associated with enstatite. For Mer_1, we also ran experiments using a mix of different sulfur sources. Mer_1 + FeS,S still contained enstatite as the liquidus mineral at $T = 1500\,°\text{C}$, and the melt later saturated with enstatite + forsterite + clinopyroxene at $T = 1450\,°\text{C}$. Lastly, anhedral quartz occurred at $T = 1400\,°\text{C}$ (Fig. 5b). In contrast, Mer_1 + S contained silicate melt saturated with enstatite + forsterite + clinopyroxene + quartz at $T = 1500\,°\text{C}$. In Mer_2(20), enstatite + forsterite + clinopyroxene + quartz co-crystallized at $T = 1350\,°\text{C}$. Forsterite later disappeared at $T = 1325\,°\text{C}$. Forsterite was small, rare, and usually surrounded by small (2–20 µm), euhedral crystals of enstatite (Fig. 5d). Clinopyroxene was small and often displayed elongated, needle–like textures (Fig. 5e). Quartz appeared as relatively large crystals (5–50 µm), always with rounded edges. In Mer_2(10), enstatite + forsterite + clinopyroxene + quartz were the cotectic assemblage at $T = 1300\,°\text{C}$. Forsterite was destabilized at $T = 1250\,°\text{C}$. Lastly, Mer_3 runs contained an assemblage of quartz, plagioclase, and clinopyroxene starting at $T = 1250\,°\text{C}$ (Table 3). Quartz crystals were large (5–70 µm), whereas clinopyroxene crystals were small (< 10 µm; Fig. 5f). Plagioclase crystals were small (< 10 µm), tabular, and always found as clusters (Fig. 5f). All SiO_2 phases featured in our experiments fall in the quartz stability field (Presnall, 1995). Our experimental samples also contained metal and sulfide phases. Mer_1 contained Si-bearing Fe metal (Fig. 5a) surrounded first by a thick liquid FeS layer, then by a small (Mg,Fe,Ca)S veneer. Among experiments with different sulfur sources, Mer_1 + FeS,S mostly contained sulfide globules of unmixed FeS and (Mg,Fe,Ca)S. At 1400 °C, we also observed pure Si metal. Conversely, Mer_1 + S only contained excess Si metal globules. We also identified some small euhedral Cr sulfide crystals at 1450 °C (Fig. 5c). We are not aware of any other experimental work reporting this phase, although Cr-bearing sulfides have been reported in chondritic meteorites (Ma et al., 2011). Mer_2(20) mostly exhibited liquid FeS and (Mg,Fe,Ca)S droplets. Si-bearing Fe metal (Fig. 5d) and Si metal globules appeared at $T = 1400\,°\text{C}$. Mer_2(10) contained mostly Si metal and liquid FeS. Fe metal was very rare in our experiments, with only one small Si-free globule observed in only one sample (A462).

5.2 Chemical composition of silicate, metal, and sulfide phases

Quantitative analyses performed on the silicate glasses are shown in Table 4. Experimental liquid lines of descent (LLDs) are shown in Figures 6 and S6. The Si content constantly increased (26–37 wt%, Fig. 6a) from 1550 to 1100 °C, whereas the Mg content steadily dropped (15–0 wt%, Fig. S6a). Na was also progressively enriched in the glass (1–6 wt%, Fig. 6d) with decreasing temperature. S content decreased from 1550 to 1250 °C (no S was added to experiments run at < 1250 °C, Fig. S6f). The difference in temperature between the appearance of quartz when different S sources are added in Mer_1 (Table 3) might be a cause of the differing Si content in the melt (Table 4), which is affected by sulfur speciation. The glass in the more reduced experiment Mer_2(20) contained 2.0–4.5 wt% S, whereas that in the more oxidized experiment Mer_2(10) contained 0–1 wt% S. Both Al and Ca were enriched in the glass from 1550 to 1250 °C, but were then depleted at lower temperatures (Fig. 6b–c) due to the saturation of plagioclase and clinopyroxene. More Ca was present in Mer_2 when 10 wt% Si was added than when 20 wt% Si added (Fig. 6c). This was likely the result of more Ca partitioning into the sulfide phases at the more reduced conditions in Mer_2(20). In all experiments, olivine and orthopyroxene matched their Mg endmember compositions (forsterite and enstatite, respectively). We only observed variations in CaO and Al_2O_3 contents in the enstatite composition over the range of starting materials investigated: both CaO (0.2–2.7 wt%) and Al_2O_3 contents (1.2–6.6 wt%) increased in enstatite with decreasing temperature (Saracino et al., 2026). In Mer_1 and Mer_2, most clinopyroxene crystals were too small for compositional analysis, with the exception of a few crystals at 1250 °C (A469). In Mer_3, clinopyroxene crystals were larger and contained 3–10 wt% Al_2O_3, 11–19 wt% MgO, 20–22 wt% CaO, and 0.7–1.8 wt% Na_2O. The average clinopyroxene composition was $Wo_{48}En_{52}$ (Fig. S7). Plagioclase was only observed in Mer_3(0) and became more sodic with decreasing temperature (An_{84} to An_{56}, where An = molar Ca/[Ca + Na]). The compositions of metals and sulfides are reported in Saracino et al. (2026). Fe metallic alloys in Mer_1 + FeS contained 83–87 wt% Fe, 6–10 wt% Si, and 0.2–0.8 wt% S. Metal alloy in Mer_2(20) + FeS contained 82–87 wt% Fe, 13–20 wt% Si, and 0.1–0.3 wt% S. In Mer_2(10) + FeS we observed a single small Fe metal globule containing ∼ 93 wt% Fe, 0 wt% Si, and ∼ 1.7 wt% S in a single run at 1300 °C.

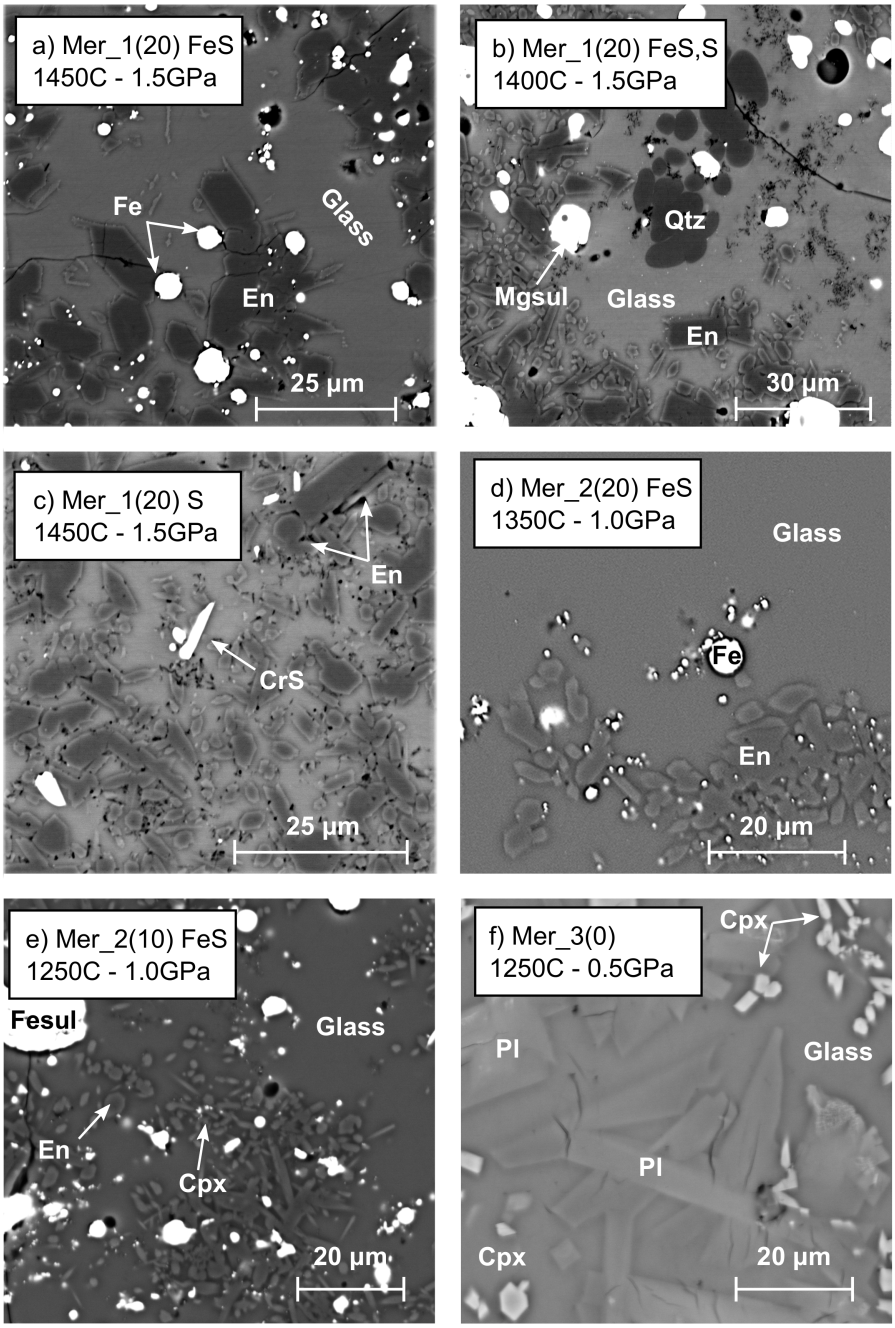

Figure 5. Representative backscattered electron images of experimental runs. (a) A396. Orthopyroxene crystals and small needle–like clinopyroxene crystals surrounded by silicate glass. The bright rounded features are Fe metal globules. (b) A405. Rounded quartz crystals together with euhedral enstatite in silicate glass. The bright phases are Mgsul globules. (c) A402. Orthopyroxene crystals (dark) and small bright Cr sulfide crystals surrounded by silicate glass. (d) A431. Small orthopyroxene crystals in silicate glass. The bright rounded features are FeS + (Mg,Fe,Ca)S globules. (e) A469. Small elongated crystals of clinopyroxene surround darker orthopyroxene. The bright rounded features are FeS globules. (f) A477. Small tabular plagioclase crystals and small grains of clinopyroxene. Abbreviations: Fo, forsterite; En, enstatite; Cpx, clinopyroxene; Qtz, quartz; Pl, plagioclase; Fe, Fe metal; Mgsul, (Mg,Fe,Ca)S.

FeS in Mer_1 contained 51–57 wt% Fe, 36–42 wt% S, 2–6 wt% Cr, and 0.7–4.7 wt% Ti. Troilite in Mer_2 had a higher Fe content (60–64 wt%) and lower S (34–38 wt%), Cr (0.2–0.9 wt%), and Ti contents (< 1.7 wt%).

5.3 Magma ocean modeling parameterization

The experimentally determined phase relations (Table 3) were used to mimic the fractional crystallization of the MMO. We calculated the cotectic proportions of mineral phases in order to model melt differentiation consistent with the experimental LLDs (Table 4). The cotectic proportions of phases used in our modeling are listed in Section S.8

Table 3. Experimental run conditions and relative phase assemblages of the experiments. Oxygen fugacity was calculated after Cartier et al. (2014) and is expressed relative to the iron–wüstite (ΔIW) solid buffer. *For experiments that do not saturate SiO_2 phases, oxygen fugacity was calculated following the method of Saracino et al. (2025). **For runs where no Si-bearing Fe metal is present, oxygen fugacity was calculated following the sulfur solubility model of Namur et al. (2016b). Abbreviations: Fo, forsterite; En, enstatite; Cpx, clinopyroxene; Qtz, quartz; Pl, plagioclase; Fe, Si–bearing Fe metal; Si, Si metal; Fesul, FeS; Mgsul, (Mg,Fe,Ca)S; Crsul, CrS.

Run	T (°C)	P (GPa)	Duration (hrs)	Silicate phases	Metals and sulfides	ΔIW[a]
Mer_1(20) + 20FeS						
A399	1525	1.5	02:00	Glass	Fe, Fesul, Mgsul	-5.8*
A397	1500	1.5	02:30	Glass, En	Fe, Fesul, Mgsul	-5.9*
A396	1450	1.5	03:00	Glass, En, Fo, Cpx	Fe, Fesul, Mgsul	-6.3*
A404	1400	1.5	03:30	Glass, En, Fo, Cpx	Fe, Fesul, Mgsul	-6.7*
Mer_1(20) + 10FeS,10S						
A401	1500	1.5	01:30	Glass, En	Fesul, Mgsul	
A400	1450	1.5	02:00	Glass, En, Fo, Cpx	Fesul, Mgsul	
A405	1400	1.5	02:30	Glass, En, Cpx, Qtz	Si, Fesul, Mgsul	
Mer_1(20) + 15S						
A403	1500	1.5	01:30	Glass, Fo, En, Cpx, Qtz	Si	
A402	1450	1.5	02:00	Glass, Fo, En, Cpx, Qtz	Si, Crsul	
Mer_2(20) + 20FeS						
A431	1350	1.0	00:30	Glass, En, Fo, Cpx, Qtz	Fe, Si, Fesul, Mgsul	-7.2
A444	1325	1.0	00:45	Glass, En, Cpx, Qtz	Fe, Si, Fesul, Mgsul	-7.9
A441	1300	1.0	01:00	Glass, En, Cpx, Qtz	Fe, Si, Fesul, Mgsul	-8.1
A445	1275	1.0	01:15	Glass, En, Cpx, Qtz	Fe, Si, Fesul, Mgsul	-8.4
A432	1250	1.0	01:30	Glass, En, Cpx, Qtz	Fe, Si, Fesul, Mgsul	-8.4
Mer_2(10) + 17FeS						
A462	1300	1.0	01:00	Glass, En, Fo, Cpx, Qtz	Fe, Si, Fesul	-3.7**
A461	1275	1.0	01:15	Glass, En, Fo, Cpx, Qtz	Si, Fesul	-3.9**
A469	1250	1.0	01:30	Glass, En, Cpx, Qtz	Si, Fesul	-3.7**
Mer_3(0)						
A477	1250	0.5	00:50	Glass, Cpx, Qtz, Pl		
A473	1200	0.5	01:00	Glass, Cpx, Qtz, Pl		
A475	1175	0.5	01:10	Glass, Cpx, Qtz, Pl		
A486	1150	0.5	03:50	Glass, Cpx, Qtz, Pl		
A487	1125	0.5	04:00	Glass, Cpx, Qtz, Pl		

(Table S2 of the Supplementary Material). We used temperature as the main criterion to define the saturation or the destabilization of solid phases in the growing cumulate pile. We developed a S-free liquid thermometer based on experimental studies of Mercury-like mantle compositions (Charlier et al., 2013; Namur et al., 2016a; Namur and Charlier, 2017; Saracino et al., 2025, Figs S8, S9 in Section S.7) and applied a correction for the depression of the liquidus temperature in the presence of sulfur (Saracino et al., 2025, Section S.7). The phase assemblages considered in our magma ocean modeling as a function of temperature are reported in Section S.9 (Fig. S10, Table S3). The densities of crystals in the cumulate pile were determined at the solidus temperature derived by fitting the solidi of the evolving MMO liquid as determined using MAGEMin (Riel et al., 2022). The effects of temperature and pressure on mineral densities were calculated with a third-order Birch-Murnaghan equation of state. The parameters used in the calculation of mineral densities are reported in the Supplementary Material (Table S1 in Section S.1).

6 Discussion

6.1 MMO evolution and the lithology of the cumulate pile

The evolution of the modeled MMO liquids for both Mer8 and Mer15 and a comparison with the experimental melts are reported in Figure 7. As a first approximation, we assumed that no trapped liquid is present in the growing cumulate assemblage so that $X_{Liq}^{Mush} = 0$ in Equation 1. The influence of Mg- and Ca-rich sulfides on the evolution of the MMO liquid is also shown (discussed further in Section 6.3). The crystallization sequence of Mer8 and Mer15 as MMO bulk compositions is shown in Figure 8 as a function of depth. In Mer8, the MMO solidification starts with the formation of a ~90 km thick basal orthopyroxenitic layer (Fig. 8a), whereas Mer15 forms a ~300 km thick dunitic basal layer (Fig. 8b). The residual melt of Mer8 becomes co-saturated in forsterite and enstatite at $F = 0.81$, whereas Mer15 reaches the forsterite-enstatite cotectic at $F = 0.38$. As also shown in Figure 2 for Mer15, a thick dunite layer is produced before the MMO residual liquid saturates enstatite

Table 4. Electron microprobe measurements of experimental silicate glasses. 1σ standard deviations are shown in italic. Abbreviations: No, number of measurements; <dl, below detection limit. *Oxygen was calculated by stoichiometry. **An excess of O^{2-} is calculated as not all Mg^{2+} or Ca^{2+} being bonded with O^{2-}, but also with S^{2-} requiring correction of the total.

Run	T (°C)	P (GPa)	No	Composition of silicate glasses (wt%)												
				Si	Ti	Al	Fe	Mn	Mg	Ca	Na	K	S	O*	S=O**	Total
Mer_1(20) + 20FeS																
A399	1525	1.5	11	26.20	< dl	4.85	0.23	0.21	13.99	3.09	2.34	0.25	5.23	45.70	2.61	99.48
1σ				*0.21*		*0.05*	*0.04*	*0.05*	*0.31*	*0.23*	*0.11*	*0.03*	*0.10*			
A397	1500	1.5	10	26.36	< dl	5.51	0.30	0.16	12.67	3.51	2.57	0.30	5.65	45.86	2.82	100.08
1σ				*0.27*		*0.07*	*0.06*	*0.05*	*0.20*	*0.24*	*0.09*	*0.02*	*0.22*			
A396	1450	1.5	10	26.86	< dl	6.59	0.32	< dl	9.78	4.17	3.36	0.38	5.74	45.98	2.86	100.31
1σ				*0.31*		*0.09*	*0.04*		*0.17*	*0.07*	*0.07*	*0.02*	*0.13*			
A404	1400	1.5	10	28.38	< dl	7.28	0.26	< dl	6.62	4.47	3.80	0.46	5.08	46.48	2.54	100.28
1σ				*0.23*		*0.10*	*0.03*		*0.10*	*0.08*	*0.05*	*0.03*	*0.11*			
Mer_1(20) + 10FeS,10S																
A401	1500	1.5	11	27.22	< dl	4.81	0.26	< dl	13.06	2.55	2.02	0.21	6.85	45.83	3.42	99.39
1σ				*0.27*		*0.05*	*0.03*		*0.10*	*0.06*	*0.07*	*0.03*	*0.13*			
A400	1450	1.5	12	28.12	< dl	5.64	0.29	< dl	11.10	2.95	2.35	0.24	6.81	46.57	3.40	100.67
1σ				*0.23*		*0.05*	*0.06*		*0.12*	*0.14*	*0.09*	*0.01*	*0.13*			
A405	1400	1.5	10	29.23	< dl	6.80	0.24	< dl	7.26	3.36	3.02	0.31	5.77	46.74	2.88	99.85
1σ				*0.22*		*0.10*	*0.05*		*0.26*	*0.11*	*0.12*	*0.02*	*0.23*			
Mer_1(20) + 15S																
A403	1500	1.5	10	28.34	0.16	4.94	0.02	< dl	12.73	2.63	1.33	0.14	5.39	46.74	2.69	99.72
1σ				*0.22*	*0.05*	*0.03*	*0.02*		*0.18*	*0.06*	*0.06*	*0.02*	*0.14*			
A402	1450	1.5	7	27.49	0.22	6.37	0.01	< dl	9.83	3.69	1.47	0.14	5.31	45.64	2.65	97.51
1σ				*0.40*	*0.03*	*0.09*	*0.02*		*0.53*	*0.18*	*0.05*	*0.02*	*0.22*			
Mer_2(20) + 20FeS																
A431	1350	1.0	17	28.55	< dl	7.86	0.32	< dl	7.17	3.47	3.53	0.33	4.19	47.04	2.09	100.36
1σ				*0.32*		*0.26*	*0.09*		*0.29*	*0.17*	*0.11*	*0.02*	*0.09*			
A444	1325	1.0	10	29.30	< dl	8.62	0.15	< dl	6.20	3.63	2.55	0.34	3.82	47.61	1.90	100.32
1σ				*0.44*		*0.26*	*0.10*		*0.20*	*0.19*	*0.07*	*0.01*	*0.07*			
A441	1300	1.0	18	29.32	< dl	8.47	0.48	< dl	4.76	3.58	3.94	0.40	3.58	47.10	1.78	99.83
1σ				*0.42*		*0.27*	*0.20*		*0.29*	*0.16*	*0.13*	*0.03*	*0.13*			
A445	1275	1.0	12	29.80	< dl	8.82	0.93	< dl	3.67	3.61	4.40	0.45	3.01	47.59	1.50	100.79
1σ				*0.75*		*0.54*	*0.15*		*0.25*	*0.41*	*0.12*	*0.03*	*0.16*			
A432	1250	1.0	10	31.47	< dl	8.54	0.48	< dl	2.55	3.38	4.81	0.57	2.12	48.15	1.06	101.00
1σ				*0.69*		*0.19*	*0.07*		*0.28*	*0.47*	*0.20*	*0.04*	*0.22*			
Mer_2(10) + 17FeS																
A462	1300	1.0	10	30.49	< dl	8.67	0.40	< dl	3.43	4.81	3.75	0.41	0.54	48.11	0.27	100.36
1σ				*0.44*		*0.21*	*0.04*		*0.14*	*0.19*	*0.22*	*0.03*	*0.06*			
A461	1275	1.0	9	31.12	< dl	8.65	0.42	< dl	2.64	4.30	3.91	0.46	0.53	48.19	0.26	99.95
1σ				*0.51*		*0.20*	*0.15*		*0.18*	*0.28*	*0.12*	*0.04*	*0.10*			
A469	1250	1.0	10	30.46	0.18	9.00	0.43	< dl	2.73	4.72	3.75	0.43	0.39	47.94	0.19	99.83
1σ				*0.38*	*0.05*	*0.21*	*0.09*		*0.08*	*0.18*	*0.09*	*0.04*	*0.08*			
Mer_3(0)																
A477	1250	0.5	6	34.41	0.07	7.43		0.06	1.35	2.44	4.66	0.59		49.51		100.54
1σ				*0.45*	*0.05*	*0.24*		*0.01*	*0.03*	*0.08*	*0.12*	*0.02*				
A473	1200	0.5	9	34.79	0.06	7.54		0.08	0.64	2.65	5.02	0.68		49.79		101.24
1σ				*0.35*	*0.09*	*0.37*		*0.02*	*0.02*	*0.17*	*0.60*	*0.02*				
A475	1175	0.5	12	36.07	0.09	6.75		0.08	0.58	2.12	5.04	0.73		50.34		101.80
1σ				*0.45*	*0.09*	*0.31*		*0.01*	*0.05*	*0.33*	*0.25*	*0.03*				
A486	1150	0.5	9	35.98	0.05	6.92		0.06	0.42	2.27	5.21	0.75		50.36		102.02
1σ				*0.49*	*0.03*	*0.26*		*0.02*	*0.02*	*0.22*	*0.20*	*0.01*				
A487	1125	0.5	10	36.47	0.12	6.56		0.07	0.40	1.90	5.17	0.83		50.50		102.02
1σ				*0.45*	*0.10*	*0.33*		*0.02*	*0.02*	*0.18*	*0.18*	*0.02*				

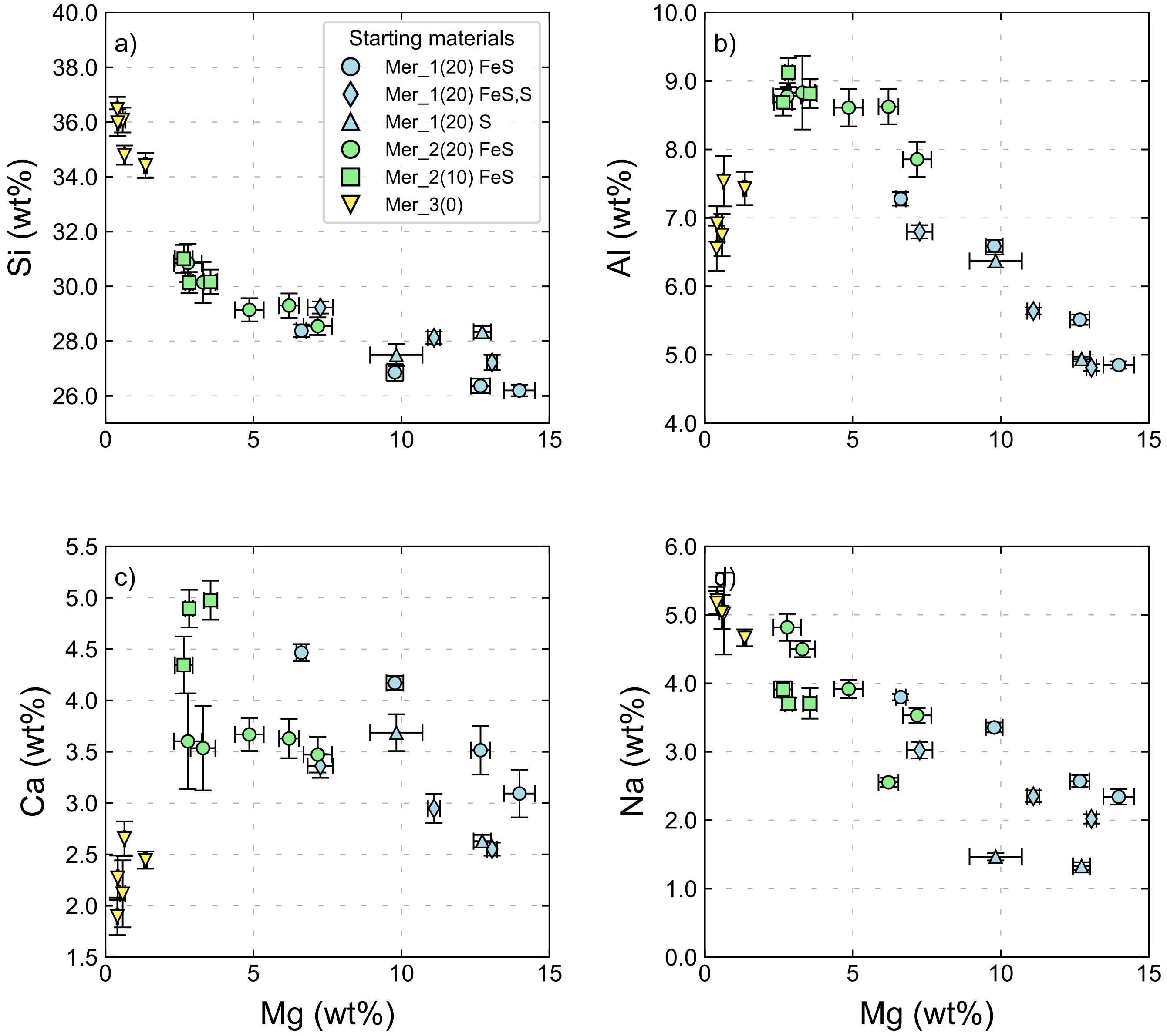

Figure 6. Evolution of Si, Al, Ca, and Na concentrations (wt%) in the silicate glass as a function of the Mg content in the glass. Vertical and horizontal bars refer to 1σ standard deviations (the smallest 1σ values are smaller than the symbol size).

too. Here, the compositions of the residual melts from sulfide-saturated Mer8 and Mer15 become similar (Fig. 7). Over this range of F (1.00–0.81 for Mer8 and 1.00–0.38 for Mer15), Si, Al, and Ca contents increase in the melt and the Mg content decreases due to the formation of enstatite and/or forsterite (Fig. 7b). Clinopyroxene is the next phase to appear at $F = 0.40$ in Mer8 and $F = 0.35$ in Mer15. Forsterite-enstatite-clinopyroxene assemblages are then followed by the appearance of quartz at $F = 0.24$ in Mer8 and at $F = 0.28$ in Mer15. Forsterite is stable until $F = 0.15$ in Mer8 and until $F = 0.21$ in Mer15, after which it disappears. Plagioclase finally crystallizes at $F = 0.14$ in Mer8 and $F = 0.19$ in Mer15, when enstatite becomes unstable. The formation of plagioclase is accompanied by a depletion of both Ca and Al in the residual liquids of both Mer8 and Mer15 (Fig. 7c,d). Crystallization models were stopped at $F = 0.12$, as we do not have experimental constraints at lower F.

Here, we compare our models with the crystallization sequences modeled by Brown and Elkins-Tanton (2009) and Mouser and Dygert (2023). We rescaled their crystallization sequences to our updated MMO depths to directly compare the models (Fig. 9; the unscaled figure is Figure S11 in the Supplementary Material).

The model of Mouser and Dygert (2023) shows a basal dunite layer, as we obtained for our Mer15 composition (Fig. 9b,c). This is caused by the similar starting Mg/Si ratio of Mer15 and the modified silicate composition of the CH chondrite (Fig. 1). The forsterite cumulate in Mer15 is nonetheless more than double the thickness of their basal layer. We also observe that the most evolved products differ substantially (Fig. 9a–c). The lithologies that we obtained based on our experiments include quartz at depths shallower than ∼140–120 km, whereas their model includes quartz-free assemblages at those depths. Our modeled sequence shows that a magma ocean composition with a high starting

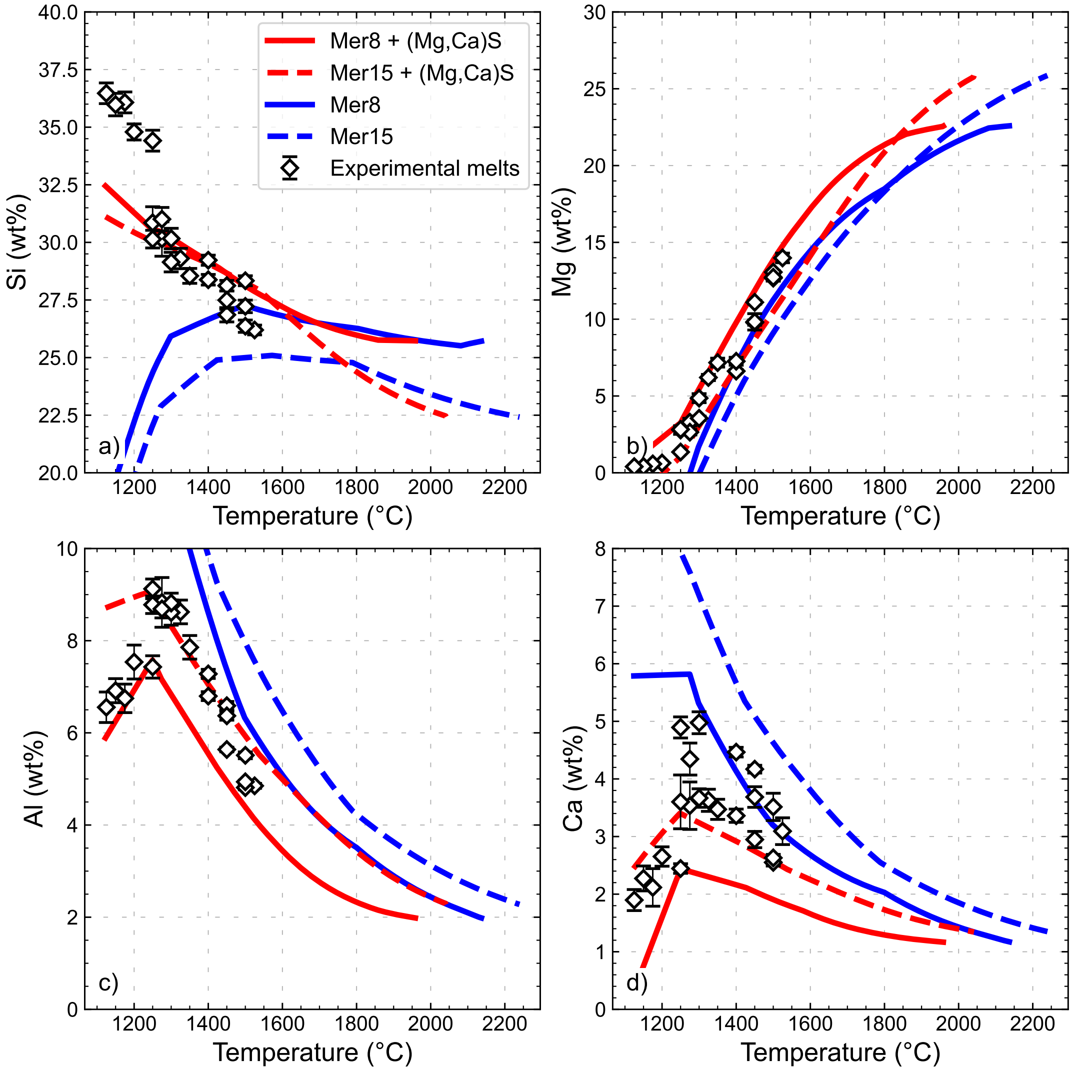

Figure 7. Variations of major element contents (a) Si, (b) Mg, (c) Al, and (d) Ca (expressed in wt%) as a function of temperature (°C), as obtained with our magma ocean model for Mer8 (solid lines) and Mer15 (dashed lines) under both sulfide-saturated (red lines) and sulfide-free (blue lines) conditions. Also shown for comparison are the experimentally determined silicate melt compositions (and relative errors; white diamonds) as listed in Table 4.

Mg/Si ratio (> 0.8) can produce a large variety of residual liquid compositions (45–75 wt% SiO_2 and 40–0 wt% MgO) through fractional crystallization (Fig. 7).

Although the models of Brown and Elkins-Tanton (2009) were based on an older estimate of the size of Mercury's core, a few considerations can be drawn from our comparison. First, none of their models produce a basal orthopyroxenite layer as produced from our Mer8 composition (Fig. 9d–g), although the Mg/Si ratios of their starting compositions (0.9–1.1 with one exception) are comparable to ours (0.8–1.2). The only major difference is therefore the absence of S in their models, which allows olivine to appear in all their basal layers because sulfur tends to favor orthopyroxene over olivine (Namur et al., 2016a; Saracino et al., 2025). Second, clinopyroxene saturation occurs at around $F = 0.50$–0.40 in their models, similar to clinopyroxene occurring at $F = 0.40$–0.35 in our models. Sulfur speciation has been shown to decrease the activity of CaO in silicate melts, delaying the formation of clinopyroxene (Anzures et al., 2020). Compared to S-free models from the literature, our S-bearing models indicate that this effect might not be as strong as previously suggested.

The different scenarios in the models of Brown and Elkins-Tanton (2009) also suggest that garnet and dense opaque phases (chromite, ilmenite) may have been stable in the MMO. Experiments at 7 GPa on the same compositions used herein (Xu et al., 2024) feature pyrope garnet at low melting fractions of $F = 0.20$–0.30. Garnet is thus a near-solidus phase and is not expected to fractionate from an evolving MMO near its liquidus. The production of high density, opaque minerals (ilmenite, chromite) at lower liquid fractions (Brown and Elkins-Tanton, 2009) is also not supported by our experiments. The paucity of Cr and Ti at the surface of Mercury (Nittler et al., 2011, 2018, 2023; Peplowski et al., 2011; Cartier et al., 2020), coupled with the more chalcophile behavior displayed by both Cr and Ti in reduced conditions (Cartier et al., 2020; Steenstra et al., 2020b), preclude those elements as being important to mineral formation in the MMO within the P-T-fO_2 range investigated herein.

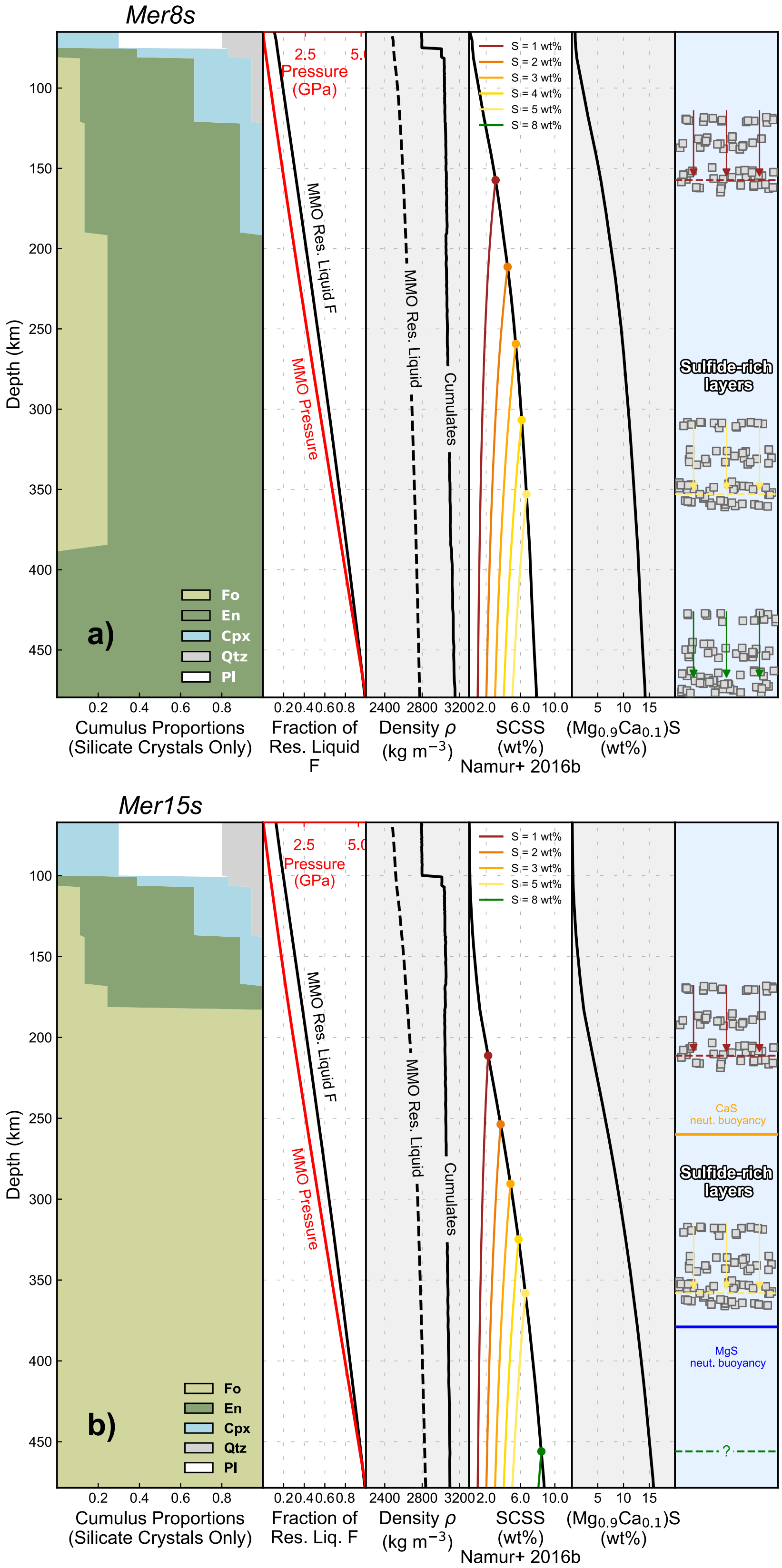

Figure 8. Crystallization sequence of S-bearing (a) Mer8 and (b) Mer15 starting materials as a function of MMO depth (km). Also shown are the variations of the melt fraction F, pressure P, the densities of the cumulates (solid black line) and the residual melt (dashed black line), the sulfur content at sulfide saturation (SCSS), the relative calculated amount of (Mg,Ca)S as a function of depth, and the potential locations (in terms of depth) of sulfide-rich cumulates. Abbreviations: Fo, forsterite; En, enstatite; Cpx, clinopyroxene; Qtz, quartz; Pl, plagioclase.

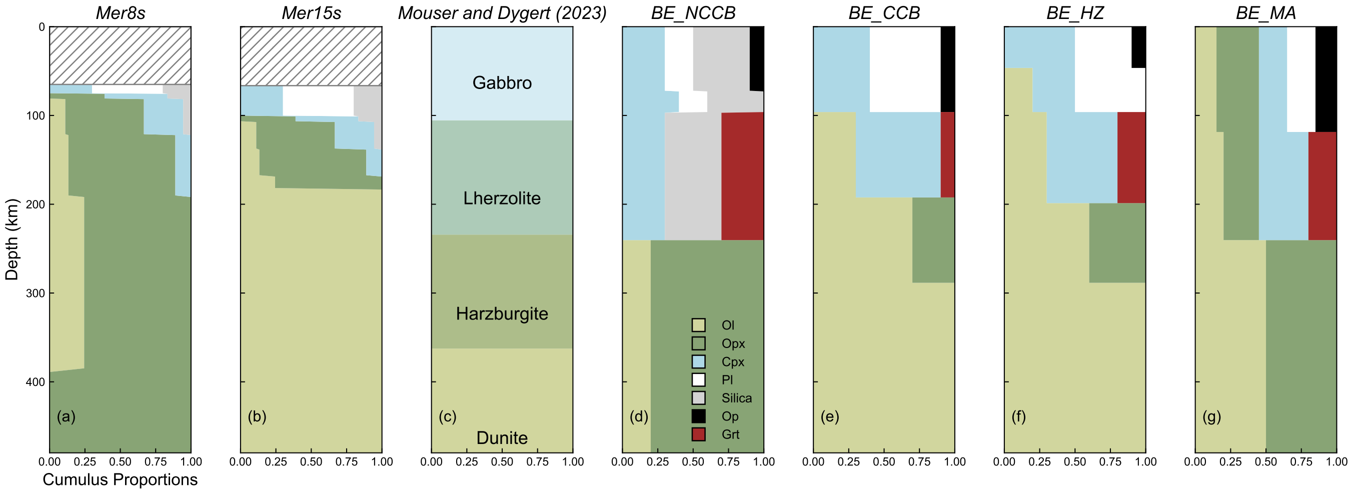

Figure 9. Comparison of MMO crystallization sequence models. The depths have been scaled for comparison. (a) Mer8 and (b) Mer15 from this study. The uppermost dashed regions refer to the unmodeled part of the crystallization sequences. (c) Pre-mantle overturn crystallization sequence of Mouser and Dygert (2023). (d) Starting CB chondrite composition (Weisberg et al., 2000; Lauretta et al., 2007) with non-chondritic Si/Mg calculated by Brown and Elkins-Tanton (2009). (e) Starting CB chondrite (Weisberg et al., 2000, 2001; Lauretta et al., 2007) with chondritic Si/Mg calculated by Brown and Elkins-Tanton (2009). (f) Starting Earth mantle composition based on measurements of fertile lherzolites (Hart and Zindler, 1986) calculated by Brown and Elkins-Tanton (2009). (g) Model composition of Earth calculated from a nebular condensation model (Morgan and Anders, 1980) calculated by Brown and Elkins-Tanton (2009). The thicker mantles in the models of Brown and Elkins-Tanton (2009) were originally calculated for a ~ 1800 km core radius (Riner et al., 2008), but are scaled to the updated MMO stratigraphy determined herein for comparison. Abbreviations: Ol, olivine; Opx, orthopyroxene; Cpx, clinopyroxene; Silica, SiO_2 phases; Pl, plagioclase; Op, opaques; Grt, garnet.

6.2 Refractory and fertile mantles: implications for crustal production

The lithological evolution of Mercury's primordial mantle impacts mantle melting conditions and the production of partial melts, eventually influencing the compositions of surface lavas. Indeed, widespread volcanism on Mercury generated its diverse geochemical regions (Head et al., 2011; Weider et al., 2015). These regions have been shown to be the product of different degrees of partial melting of a heterogeneous mantle (Charlier et al., 2013; Namur et al., 2016b; Wang et al., 2022). Charlier et al. (2013) originally proposed different melting sources for two chemically distinct surface regions approximately in the southern hemisphere (termed the 'intercrater plains-highly cratered terrains' or IcP-HCT) based on the first XRS data from the MESSENGER spacecraft. They suggested that the two geochemically distinct units G1 (low Al_2O_3 and high CaO, MgO) and G2 (high Al_2O_3 and low CaO, MgO) were the product of low-pressure (< 10 kbar) partial melting of lherzolitic and harzburgitic mantle sources, respectively. As new geochemical data became available (Weider et al., 2015), Namur et al. (2016a) proposed that the geochemical terrains had equilibrated at low pressure (< 15 kbar) following adiabatic decompression of lherzolitic mantles differing by their clinopyroxene fraction. In particular, they found that MgO-rich lavas were generated by a high degree of partial melting ($F = 0.35 \pm 0.03$) starting deeper in the mantle (~ 360 km depth, corresponding to ~ 4.5 GPa) and at higher temperatures (~ 1720 °C) compared to Northern Volcanic Plain lavas ($F = 0.27 \pm 0.04$) that formed at shallower depths (~ 160 km) and lower temperatures (~ 1435 °C). Similarly, Wang et al. (2022) showed that the geochemical region characterized by high Mg/Si (the 'high Mg region' or HMR) may have originated from multiple mantle sources characterized by jagged, irregular boundaries, whose melting was likely favored by local thermal anomalies early in the planet's history (> 4.1 Ga). Melting experiments on a synthetic EH4 composition at 0.5–5.0 GPa (relevant to the petrogenesis of Mercury's surface lavas) showed that melting of a single enstatite-rich chondritic composition can produce a variety of silicate melt compositions, from high-Mg melts at high pressure (2–5 GPa) to silica-rich silicate melts at low pressure (0.5–1 GPa; Boujibar et al., 2025). They also argued that Mercury's mantle is mainly pyroxenitic in composition due to the large stability field of orthopyroxene in sulfur-bearing systems.

Studying the primordial mantle of Mercury as produced from a fractionating magma ocean is paramount to understanding the melting sources responsible for the formation of the surface lavas. Importantly, previous melting studies overlooked that certain portions of the primordial mantle would have been more refractory to melting. Our results show that a refractory mantle is produced in the lower cumulate pile, which could be solely forsterite, solely enstatite, or include both phases. In the upper-MMO sequence, a fertile mantle forms when clinopyroxene becomes part of the cumulus assemblage. The formation of clinopyroxene-bearing mantle lithologies starts at around 160–190 km depth (Fig. 10). Experimental studies have shown that a refractory mantle made of an olivine + orthopyroxene assemblage would melt congruently between 1680 °C at 1.2 GPa and 1780 °C at 2.5 GPa (Chen and Presnall, 1975). Conversely, a mantle containing olivine + orthopyroxene + clinopyroxene would start melting between 1310–1320 °C at 1.2 GPa and 1520 °C at 2.5 GPa (Walter and Presnall, 1994).

Because of the contrasting fusibility of the refractory and fertile mantles, it is expected that the fertile mantle was the dominant contributor to crustal production via partial melting. Here, we evaluate if the fertile mantle produced by MMO crystallization can actually produce the relatively thick volcanic surface of Mercury by partial melting alone. We consider the thickness of the fertile mantle to be 140 km. We then calculate the volume of the silicate shell corresponding to the fertile reservoir as:

$$V_{Fertile\ Mantle} = \frac{4}{3}\pi\left(R^3_{Mercury} - R^3_{Core+Refractory\ Mantle}\right) \tag{11}$$

where $V_{Fertile\ Mantle}$ is the volume of the fertile mantle, $R_{Mercury}$ is the radius of Mercury (2440 km), and $R_{Core+Refractory\ Mantle}$ is the radius of the core plus the refractory reservoir of Mercury (2300 km). From this, we can calculate the volume of melt produced at a fixed melt fraction F, and the relative thickness it would produce as lavas after extraction and cooling at the surface. We first consider a minimum degree of partial melting ($F = 0.30$) among estimated values in the literature (Namur et al., 2016a; Beuthe et al., 2020; Wang et al., 2022; Boujibar et al., 2025). Then we can calculate the volume of partial melt produced, and therefore the thickness of the layer that such a melt would produce at the surface (or within the crust; i.e. intrusive magmatism). We find the thickness of the volcanic crust to be 40 km, in good agreement with the estimated crustal thickness of 35 ± 17 km of Padovan et al. (2015). Higher degrees of partial melting (up to 0.70 for the HMR region; Boujibar et al., 2025) have also been suggested. Higher values of F (0.50–0.60) in our models would indeed yield a crustal thickness in the range 60–80 km. The range of crustal thicknesses produced by low degrees of partial melting are well within the various estimates of the extent of the Mercurian crust (Padovan et al., 2015; Beuthe et al., 2020). Our results therefore suggest that Mercury's volcanic crust may have originated from the partial melting of the fertile mantle portion alone. It is important to note, however, that the mantle of Mercury, as formed post-MMO crystallization, might have undergone one or multiple episodes of density-driven mantle overturn (Brown and Elkins-Tanton, 2009; Mouser and Dygert, 2023), which may have refertilized deeper mantle sources capable of producing partial melts by adiabatic decompression melting (Namur et al., 2016a).

6.3 Sulfides in the mantle of Mercury

SCSS can be calculated at each incremental step of our crystallization model to track the formation of Mg- and Ca-rich sulfides. Studies investigating the MgS-CaS system show that a (Mg,Ca)S solid solution is stable over the MMO's temperature range (Pitsch et al., 2025). Under reduced conditions, SCSS sensibly decreases with temperature and is affected by the composition of the silicate melt (Namur et al., 2016b). Two end-member scenarios are usually considered when investigating the fate of sulfur in early differentiation processes on Mercury (e.g. Boukaré et al., 2019; Pirotte et al., 2023). In the first, the magma ocean was initially saturated with sulfides, allowing for sulfide phases to form at the CMB, perhaps together with an FeS layer atop the core. In the second, the MMO reached sulfide saturation later (at lower temperature) during crystallization, preventing sulfides from forming during the early stages.

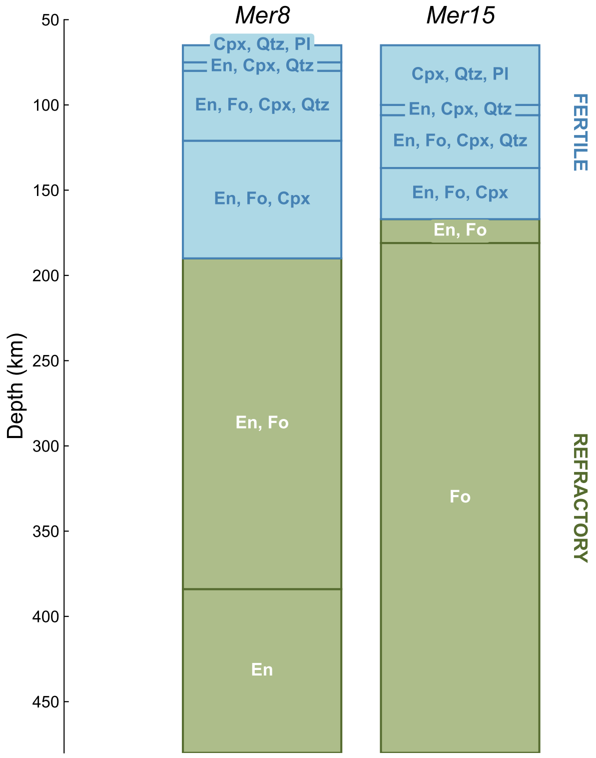

Figure 10. Refractory (green) and fertile (light blue) mantle reservoirs for sulfide-bearing Mer8 and Mer15, respectively.

To explore the potential sulfur content of the cumulate pile, we calculated SCSS using the model of Namur et al. (2016b), assuming an average mantle oxygen fugacity of $\log(fO_2) = \mathrm{IW}\text{-}5.4$ (Namur et al., 2016b) for both Mer8 and Mer15 (Fig. 8). At CMB conditions, Mer15 (SCSS ∼8.8 wt% at 2040 °C) has a higher SCSS than Mer8 (SCSS ∼7.8 wt% at 1960 °C) due to the higher temperatures and MgO concentrations of Mer15 melts. We use a range of BSMe S concentrations (1–8 wt% S) and track the onset (fraction of residual liquid) of sulfide crystallization. We treat sulfur as a fully incompatible element in the silicate melt ($D_S^{crystal/melt} = 0$). The concentration of sulfur in the melt can therefore be determined as:

$$C_{S,Liq} = C_{S,0}F^{-1} \tag{12}$$

where $C_{S,Liq}$ is the concentration of sulfur in the residual liquid and $C_{S,0}$ is the starting concentration of sulfur in BSMe. When the path of increasing sulfur content with decreasing depth (or the fraction of residual liquid) reaches the modeled SCSS, the magma ocean becomes saturated with sulfide. We observe that for 1 wt% S in the starting BSMe, sulfide saturation is attained at $F = 0.33$ (~ 160 km depth) for Mer8 and $F = 0.45$ (~ 210 km depth) for Mer15. At 5 wt% S in the BSMe, sulfide saturation occurs closer to the CMB (~ 350 km depth for Mer8 and ~ 360 km depth for Mer15). At 8 wt% S, the Mer8 MMO would be saturated with S at the onset of crystallization, whereas the Mer15 MMO would only reach sulfide saturation at ~ 450–460 km depth (Fig. 8b). At > 8.8 wt% S, the Mer15 MMO would be saturated with S at the CMB.

In Figure 8a,b, we show the potential sulfide content in the cumulate pile. As an approximation, $(Mg_{0.9}Ca_{0.1})S$ is considered as the stable sulfide phase that would form in this fO_2 range ($\Delta IW < -4.5$; Anzures et al., 2020, 2025). Different starting BSMe S contents would affect the amount of (Mg,Ca)S in Mercury's primordial mantle. For example, in Mer8, 1 wt% S in the starting silicate magma ocean would produce ~ 5.5 wt% (Mg,Ca)S at 160 km depth, whereas 5 wt% S in the magma ocean would crystallize ~ 12.0 wt% sulfides at 350 km depth. Lark et al. (2022) calculated the abundance of Mg- and Ca-rich sulfides in Mercury's mantle based on the inferred mantle S content of Namur et al. (2016b). They found that 13–20 wt% (Mg,Ca)S would crystallize from the MMO.

We also evaluate the role that 10 wt% (Mg,Ca)S could play on the evolution of the residual MMO liquid in Figure 7. Sulfide-free residual liquids (blue lines in Fig. 7), after an initial slight increase in Si (up to 25–28 wt%), become depleted in silica with progressive crystallization in both the Mer8 and Mer15 cases (with Si down to 20–15 wt%). In contrast, due to decreased proportions of crystallizing silicate minerals, sulfide-bearing liquids (red lines) show enrichments of up to ~ 32–33 wt% Si under the investigated conditions (Fig. 7a). This is supported by the composition of the experimentally determined S-bearing silicate melts (Fig. 7a). Importantly, the fate of Al and Ca changes dramatically depending on the presence or absence of sulfides (Fig. 7c,d). In accordance with our experiments, Al and Ca concentrations in sulfide-bearing liquids will first increase (up to 7–10 wt% Al and 2–4 wt% Ca) because they are hardly consumed by early forming phases (enstatite, forsterite). Then, once plagioclase crystallizes, their concentrations decrease (down to 5–9 wt% Al and 0–3 wt% Ca). Conversely, in sulfide-free liquids, we observe an enhanced enrichment of Al and Ca before plagioclase formation (> 10 wt% Al and > 5 wt% Ca). In addition, we also observe that Mg behaves similarly in the sulfide-free MMO as in its sulfide-bearing counterparts (Fig. 7b).

In this study, we modeled the crystallization of MMO considering Mg-dominated sulfides (plus Ca), which is considered to be the main sulfide phase stable in the range of oxygen fugacities investigated in this study (Anzures et al., 2020, 2025). It is, however, important to add that Mercury's magma ocean might have segregated other sulfides containing Na, K, Ti, and Cr (Anzures et al., 2020, 2025; Mouser and Dygert, 2023). Such exotic sulfides have been also found in aubrites, enstatite-rich achondrites that might represent analogs of Mercury's surface (e.g. Cartier and Wood, 2019; Wilbur et al., 2022).

6.4 MMO density and potential mineral flotation

Determining the density of silicate melts containing sulfur requires knowledge of the nature of bonding between S and typical silicate melt cations, for which the uncertainties remain large. Silicate melts are considered to dissolve ionic S (e.g. O'Neill, 2021), although several studies have demonstrated the bonding of S with cations like Mg, Ca, Si, and Na in silicate glasses using a variety of analytical approaches (Namur et al., 2016b; Anzures et al., 2020, 2025; Pommier et al., 2023). Some of these analyses, however, were performed on quenched products, which may show differences in speciation and elemental distributions compared to silicate melts (Mysen, 1983). Under reduced conditions, anionic oxygen is partly replaced by sulfur (Fincham and Richardson, 1954); therefore, in terms of molar mass, the density of a silicate liquid containing dissolved S is slightly higher than that of a S-free silicate liquid because sulfur has roughly twice the mass of oxygen (32 vs. 16 g mol^{-1}). However, the ionic radius of S^{2-} (1.84 Å) is larger than that of O^{2-} (1.41 Å), implying a greater molar volume and thus a lower specific density of sulfur-bearing melt components. Indeed, S has a lower specific density than other typical melt components. At room temperature, the partial specific density (M_i / V_i, with M_i being the molar mass and V_i the molar volume of melt component i) of S (~ 2060 kg m^{-3}) is within the range of the specific densities of other melt components like SiO_2 or K_2O (2000–2200 kg m^{-3}), and higher than those of common volatiles (H_2O, CO_2 at 900–1400 kg m^{-3}; Lesher and Spera, 2015). In contrast, if we assume MgS and CaS as melt species in sulfur-bearing silicate melts, the bonding of S with Mg and Ca would decrease the activities, and therefore the molar fractions, of MgO and CaO species in the silicate melt, which have higher specific densities (3300–3600 kg m^{-3}) compared to S and other sulfides. Furthermore, the occurrence of MgS and CaS melt species will increase, which have specific densities of ~ 2500–2700 kg m^{-3} in their solid form (Lark et al., 2022). The densities of these species are higher than dominant melt components like SiO_2 (2200 kg m^{-3}) but lower than the specific densities of MgO and CaO.

Therefore, the densities of silicate liquids containing dissolved S should, in principle, slightly decrease. We calculated the effect of sulfur on the density of the MMO liquid (details on the procedure are reported in Section S.12). The resulting densities of the MMO calculated for Mer8 and Mer15 are shown in Figure 11. To our knowledge, this study is the first attempt to explore the impact of S on the density of reduced, Mg-rich silicate melts, although we stress that further studies specifically dedicated to understanding the volumetric properties of S and other sulfides at high temperatures and pressures are needed. Nonetheless, we importantly find that sulfur plays a major role in decreasing the density of silicate liquids. For example, around 10 wt% S dissolved in a silicate liquid would decrease the density by

$\sim 210\,\mathrm{kg\,m^{-3}}$. This effect may have serious consequences on the ability of newly formed solid phases to float in a vast magma ocean.

To investigate the possibility that minerals formed in the MMO could become buoyant, we compare the densities of the S-bearing residual liquids for both the Mer8 and Mer15 BSMe compositions with the density of solid phases as a function of depth (Fig. 11). Mineral phase densities are calculated with third-order Birch-Murnaghan equations of state in terms of density (Birch, 1947; Vander Kaaden and McCubbin, 2015) using parameters listed in Section S.1 (Table S1). We confirm that graphite has a lower density than any residual MMO melt (brown dash-dotted line in Fig. 11), and may have thus continuously contributed to the formation of the primordial graphite crust. We also observe that quartz, appearing at $F = 0.24$–0.28, is denser than the residual melts (black dashed line in Fig. 11). Plagioclase is the last mineral appearing in our models at $F = 0.14$–0.19 (purple dashed line in Fig. 11) and is also shown to be denser than the residual MMO liquid. Although we did not model the very last MMO crystallization products, we expect plagioclase to become more albitic in the last stages of MMO crystallization. We therefore plotted albite in Figure 11 (dark green dashed line), which is also denser than the residual MMO liquid. We also plot potential sulfide minerals (niningerite, MgS; blue dash-dotted line; oldhamite, CaS; orange dash-dotted line) that could have segregated from the MMO (Boukaré et al., 2019; Mouser and Dygert, 2023). For Mer8, since the beginning of MMO crystallization, the density of the MMO liquid is lower than the densities of the sulfides. If the MMO was initially sulfide saturated, we would then expect the sulfides to sink into the cumulate pile with the early formed silicates like enstatite and/or forsterite (last panel in Fig. 8a). Even in the case that sulfide saturation was attained later during MMO crystallization, the newly formed sulfides would still have been denser than the residual liquid (Fig. 8a). As for Mer15, we observe that at CMB conditions, sulfides are slightly positively buoyant with respect to the MMO liquid ($\Delta\rho^{sulfides,\ MMO} = -3$ to $-13\,\mathrm{kg\,m^{-3}}$; last panel of Fig. 8b). Gravitational phase segregation depends on several variables such as convective regimes, crystal-melt density contrast, crystal size and crystal fraction, and melt viscosity (Elkins-Tanton, 2012; Solomatov, 2015; Mouser et al., 2021). Sulfide flotation may have been hindered by turbulent convection in the magma ocean (Schmidt and Kraettli, 2022). In the case of Mer15, the density contrast between the sulfides and the magma ocean is too small to effectively segregate sulfides; in this case, sulfides would be trapped amongst the co-crystallizing forsterite minerals.

Considering a MMO of Mer15 composition saturated with sulfides at the onset of crystallization, the sulfides, whether formed before or after the sulfide density crossover, would be stored in the lower and intermediate sections of the mantle. In the alternative case where the MMO Mer15 composition is not saturated with sulfides from the onset of crystallization, sulfides would likely start forming at intermediate depths in the mantle.

As mentioned in Section 6.3, sulfides other than niningerite and oldhamite may have segregated from the MMO. Sulfides containing Na, K, Cr, Ti may have formed during MMO solidification (Anzures et al., 2025). Their appearance is further corroborated by the presence of natural sulfide phases like troilite, caswellsilverite, heideite, daubréelite, alabandite, and djerfisherite in aubrites (e.g. Keil, 2010; Wilbur et al., 2022). These differentiated meteorites are generally dominated by FeO-free enstatite, minor Na-rich plagioclase, FeO-free diopside, and forsterite (Keil, 2010). Aubrites formed under reduced conditions, which makes them good analogs of Mercury's surface (Cartier and Wood, 2019). Mineral densities of aubritic sulfides (at 1 atmosphere) are listed in Table 1 of Mouser and Dygert (2023), for which parameters needed for density calculations are lacking. Nonetheless, one important point should be noted. Except for oldhamite and niningerite modeled here (Fig. 11), these sulfides would be much denser ($\rho > 3200\,\mathrm{kg\,m^{-3}}$) than the residual MMO liquid over the entire range of pressures investigated here, plotting outside Figure 11. They would likely sink at the bottom of the residual MMO.

6.5 Implications for the storage of heat-producing elements

The primordial structure of the Mercurian mantle affected the distribution of HPEs like U, Th, and K. The partitioning of these elements between the silicate, metallic, and sulfide phases may have also been influenced by the reduced conditions during Mercury's differentiation (Boujibar et al., 2019; Pirotte et al., 2023). Elements tend to become more chalcophile and siderophile at increasingly reduced conditions (McCubbin et al., 2012; Wohlers and Wood, 2017; Boujibar et al., 2019; Steenstra et al., 2020b; Pirotte et al., 2023). A FeS layer atop the metallic core may also affect the HPE distribution and heat production (Boujibar et al., 2019; Boukaré et al., 2019), although the existence of such a layer remains debated (Smith et al., 2012; Cartier et al., 2020; Pirotte et al., 2023). Oxygen fugacity and the initial S content of the MMO have been shown to affect the storage of U in the Mercurian mantle (Boukaré et al., 2019). At low initial S contents (~ 1 wt%) and relatively oxidizing conditions (IW-4 to IW-2), sulfides remain in sufficient abundances that HPEs could be preferentially hosted in a sort of KREEPy (K, REE, and P-rich) layer in the upper mantle or, if present, in the FeS layer at the CMB. Under more reducing conditions (IW-6), sulfides are segregated in the shallow mantle of Mercury (< 96 km depth), making this region richer in HPEs. At higher initial S contents (~ 5 wt% S) and oxidizing conditions ($>$ IW-4), SCSS is low, and an FeS layer would form at the CMB, storing important amounts of HPEs (Boukaré et al., 2019). At high S contents and reduced conditions, HPEs would mostly be concentrated in the intermediate and upper mantle (< 220 km depth; see Fig. 2 in Boukaré et al., 2019).

Importantly, large uncertainties surround the HPE distribution between Mg- and Ca-rich sulfides and the silicate melt (e.g. Boukaré et al., 2019). Only Pirotte et al.

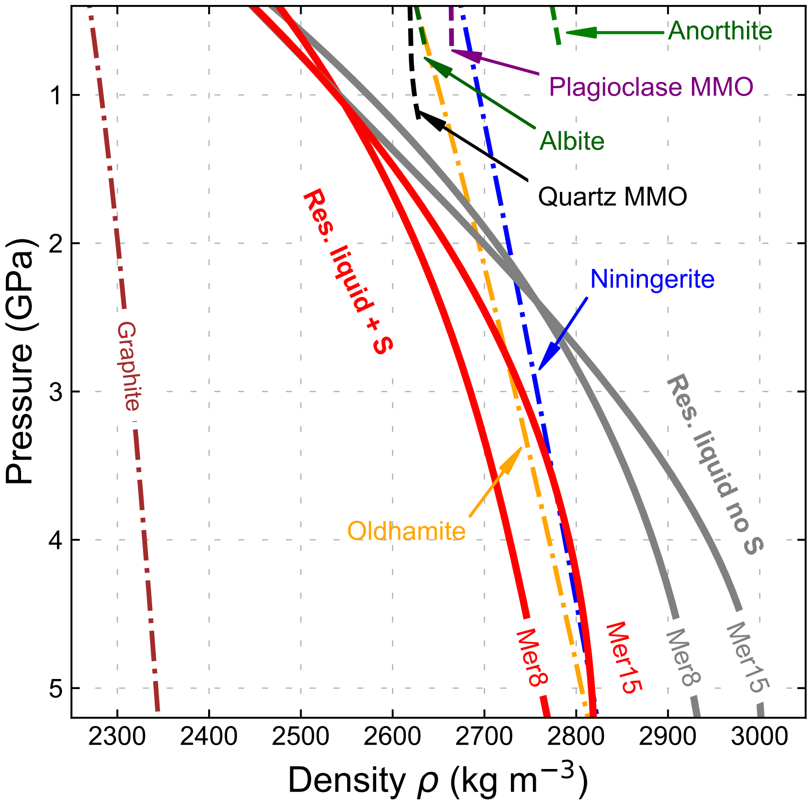

Figure 11. The densities of evolving residual MMO liquids as compared to plagioclase, quartz, graphite, and Mg-, Ca-sulfides.

(2023) recently determined the partition coefficients of HPEs between MgS and the silicate melt under reduced conditions (IW-8.5), showing the incompatible behavior of U and Th. Differences in the lattice structure between Mg- and Ca-bearing sulfides might affect the incorporation of HPEs, and particularly U and Th (Blundy and Wood, 2003). Indeed, Ca-rich sulfides have been shown to be significant U and Th carriers in enstatite achondrites (Murrell and Burnett, 1982). Rare earth elements (REEs) also partition into oldhamites found in aubrites and enstatite chondrites (Dickinson and McCoy, 1997; Ingrao et al., 2019). This hints at a potentially higher partitioning of HPEs in Ca-rich sulfides. Here we quantify HPE partitioning in the MMO for both Mer8 and Mer15 compositions considering two end-member scenarios: (i) incompatible HPEs, using $D_U^{MgCaS/Melt} = 0.5$, $D_{Th}^{MgCaS/Melt} = 0.1$ from Pirotte et al. (2023), and considering for $D_K^{MgCaS/Melt}$ an average (0.05) from the range found in Pirotte et al. (2023); (ii) compatible U and Th, assuming $D_U^{MgCaS/Melt} = D_{Th}^{MgCaS/Melt} = 2$, following the case of moderately high partition coefficients in Boukaré et al. (2019, here K was not considered as we believe it would still behave very incompatibly). The partitioning of element i between a solid phase and the silicate melt is expressed by the partition coefficient D_i, as:

$$D_i^{Crystal/Melt} = C_i^{Crystal} / C_i^{Melt} \tag{13}$$

where $C_i^{Crystal}$ is the concentration of element i in a given crystal phase, and C_i^{Melt} is the concentration of element i in the melt. The concentrations of trace elements, like HPEs, in the MMO are calculated following Rayleigh's equation for fractional crystallization (Eq. 1). We calculate the distribution of HPEs based on the estimated (Mg,Ca)S content as shown in Figure 8a,b. Partition coefficients for the silicate minerals are from White (2020). The starting U, Th, and K concentrations in the BSMe are from Pirotte et al. (2023). The concentrations of U, Th, and K in the MMO as a function of depth are reported in panel (a) of Figure 12. Furthermore, after calculating the concentration of HPEs in the evolving MMO liquid, we could also determine the HPE abundances in the cumulate assemblages. The results are reported in Figure 12b. For clarity, we only show Mer8 (Fig. 12). Plots for Mer15 are shown in Section S.13 (Fig. S13).

In scenario (i: incompatible HPEs) U, Th, and K are all incompatible, and their concentrations increase in the residual silicate liquid as the cumulate grows in thickness (red lines in Fig. 12a). We also show sulfide-free magma ocean models for comparison (grey lines in Fig. 12). The residual sulfide-bearing liquids are slightly more depleted than compared to the equivalent corresponding sulfide-free liquids, given the more compatible behavior displayed by U and Th (Fig. S14). Silicate liquids trapped in the growing cumulate might affect the trace element budget of the residual magma ocean liquid (Snyder et al., 1992; Elkins-Tanton et al., 2011). We therefore modeled the HPE budget considering 5% trapped liquid in the cumulate assemblages (dark green lines in Fig. 12). HPEs are still enriched in the residual MMO liquid as crystallization proceeds. We only observe slightly lower HPE abundances compared to sulfide-bearing liquids with no trapped melt. In scenario (ii: compatible HPEs), U and Th are still enriched in the residual MMO liquid (orange and light green lines in Fig. 12a), although to a lesser extent as compared to scenario (i), given the higher bulk partition coefficients of the sulfide-bearing cumulates (Fig. S14a). The most noticeable difference between the two scenarios is found in the HPE abundances in the cumulates (Figs 12b and S13b for Mer15). We show an increased content of U (4–8 ppb in sulfide-bearing Mer8 with no trapped liquid; 8–10 ppb in sulfide-bearing Mer8 with trapped liquid; 2–9 ppb in sulfide-bearing Mer15 with no trapped liquid; 6–10 ppb in sulfide-bearing Mer15 with trapped liquid) and, particularly, Th (32–36 ppb in sulfide-bearing Mer8 with no trapped liquid; 37–42 ppb in sulfide-bearing Mer8 with trapped liquid; 11–36 ppb in sulfide-bearing Mer15 with no trapped liquid; 24–40 ppb in sulfide-bearing Mer15 with trapped liquid) as compared to scenario (i) in the lower and intermediate mantle of Mercury (< 150–200 km depth) caused by both the higher compatible behavior of HPEs in the sulfides coupled with the higher content of sulfides calculated in the lower portions of the mantle (Fig. 8).

In general, considering both scenarios, we observe that the residual liquid of the MMO would likely contribute to forming a shallow layer that is rich in incompatible elements (Fig. 12a, Fig. S13a). A KREEP layer in the upper mantle of Mercury is therefore hypothesized, similar to the Moon (Warren and Wasson, 1979; Warren, 1988; Zhang et al., 2024). On Mercury, such a layer would be found between the late cumulates and the primary graphite crust. As regards the cumulates, we notice that the presence of sulfides combined with that of trapped melt have an effect on HPE distribution in the cumulates (Fig. 12b, Fig. S13b). Although we observe that sulfides alone will only cause a small U, Th enrichment in early cumulates (roughly a 2–5 ppb difference), the presence of trapped liquid will cause a steeper U, Th enrichment, especially in the late cumulate sequence (< 200 km depth). K is almost absent in early formed cumulates (only trapped liquid has a minor effect), and it will only be stored when plagioclase saturates.

7 Conclusions

We investigated early differentiation processes occurring during the first evolutionary stages of planet Mercury. In detail, we studied the crystallization products of a S-rich Mercurian Magma Ocean (MMO) under reduced conditions. Our major findings and their implications are summarized as follows:

- The lithology of the primordial mantle of Mercury relies heavily on the Bulk Silicate Mercury (BSMe) composition and the presence of sulfur. A BSMe with a low Mg/Si ratio and a high S content will favor the formation of an orthopyroxenite layer at the base of the primordial mantle, whereas a S-saturated BSMe with a high Mg/Si ratio will crystallize a thick forsterite basal layer.
- Sulfur strongly impacts silicate phase equilibria. S in the MMO decreases the activity of MgO and CaO in the residual liquid, slightly delaying the formation of clinopyroxene and plagioclase. In contrast, S increases the activity of SiO_2, allowing quartz to form early in the crystallization sequence.
- Due to the delayed formation of clinopyroxene and plagioclase, we showed that only a small portion of the primordial Mercurian mantle would have contributed to forming a fertile mantle reservoir.
- Sulfur plays a critical role in the chemical evolution of the MMO liquid. We showed that S-bearing silicate liquids have LLDs that are dramatically different from their S-free counterparts. Particularly, we showed that even primitive compositions with high Mg/Si will produce silica-rich, MgO-poor residual liquids.
- Sulfur also affects the density of the MMO. S-bearing silicate liquids are less dense than S-free liquids. However, further detailed studies are necessary to investigate the volumetric properties of sulfur and sulfides at high temperatures and pressures in magmatic systems.
- Graphite is likely the main mineral to float in the MMO and contribute to the formation of the primordial crust. Sulfide minerals, ranging from Mg-, Ca-bearing sulfides to more unusual compositions are generally denser than the MMO and are likely stored in the Mercurian mantle. Their distribution also depends on the bulk sulfur content of the BSMe.
- Heat-producing elements behaved incompatibly in the MMO and likely accumulated in the upper primordial mantle of Mercury. Large uncertainties remain on HPE partitioning in sulfides, so that two scenarios involving (i) incompatible HPEs and (ii) compatible HPEs were explored. If HPEs are indeed more compatible in sulfides than previously thought, the intermediate and lower mantle of Mercury might store relevant HPE amounts. Moreover, we highlight the effect of trapped liquid coupled with the presence of sulfides on the storage of HPEs in the growing cumulate sequence. We suggest that a sulfide-bearing KREEP layer, similar to that on the Moon, formed on Mercury. The presence of sulfides and trapped silicate liquid in the cumulate causes a small depletion of HPEs in the uppermost layers.

The upcoming ESA and JAXA BepiColombo mission (Benkhoff et al., 2021), and particularly the compositional and mineralogical data returned by the MERTIS, MGNS, MIXS, and SYMBYO-SIS instruments (Bunce et al., 2020; Cremonese et al., 2020; Hiesinger et al., 2020; Rothery et al., 2020; Mitrofanov et al., 2021), will be able to test our scenarios, therefore providing a revised model of Mercury's internal differentiation and crustal formation. We believe that our study represents a starting point for investigating the early differentiation processes of Mercury, and it may be also extended to exploring the early evolution of reduced, S-rich exoplanets with high core-to-mantle ratios (e.g. Santerne et al., 2018; Barros et al., 2022; Cioria et al., 2024).

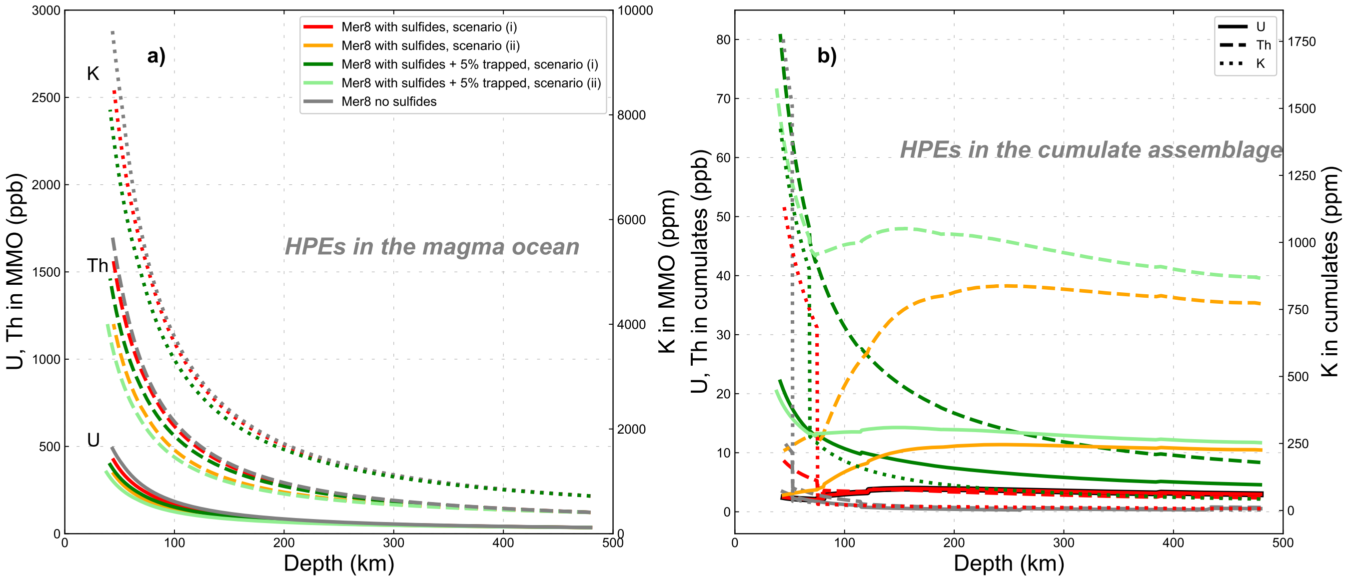

Figure 12. (a) Uranium, thorium (both ppb), and potassium (ppm) distributions in the MMO as a function of depth (km) in Mer8. Grey lines refer to sulfide-free Mer8, red lines refer to sulfide-bearing Mer8 with incompatible HPEs (more details are in Section 6.5), orange lines refer to sulfide-bearing Mer8 with compatible HPEs, dark green lines refer to sulfide-bearing Mer8, incompatible HPEs with 5 % trapped melt in the cumulate pile, and finally light green lines refer to sulfide-bearing Mer8, compatible HPEs with 5 % trapped melt. Solid lines refer to uranium (U), dashed lines refer to thorium (Th), and dotted lines refer to potassium (K). (b) Uranium, thorium (both ppb), and potassium (ppm) distributions in the growing cumulates as a function of depth (km) in Mer8.

Acknowledgements

We wish to thank Raúl Fonseca (handling editor), Nick Dygert and an anonymous reviewer for their constructive comments which improved the quality of this article. We also thank Kate Kiseeva (production editor) for aiding in the revision process. FS wishes to thank Thomas Van Gerve (KU Leuven) for his help in the use of the SEM and the EPMA. We are grateful to Robert Dennen for his careful editing of the manuscript. This article was possible thanks to the support of the National Fund for Scientific Research (FNRS, Belgium) grant FRIA 40021515 (Fund for Research Training in Industry and Agriculture). BC is a Research Associate of the Belgian Fund for Scientific Research-FNRS and acknowledges funding from the ESA PRODEX Program (Grant 4000142722). ON acknowledges support from the European Research Council (ERC) for a Consolidator Grant (IronHeart) under the European Union's Horizon (grant agreement no. 101125126).

Data, code, and outputs availability

All data and codes are available at Saracino et al. (2026): https://doi.org/10.5281/zenodo.20273496. Main text figures and tables are available for download in the online version of this article.

Use of Artificial Intelligence tools

Generative AI (ChatGPT Plus) was used to improve code structure, organize modeling scripts, and customize figures.

Competing interests

The authors declare no competing interests.

Licence agreement

References

Anzures BA, Parman SW, Milliken RE, Namur O, Cartier C, McCubbin FM, Vander Kaaden KE, Prissel K, Iacovino K, Lanzirotti A, Newville M (2025). An oxygen fugacity-temperature-pressure-composition model for sulfide speciation in Mercurian magmas. *Geochimica et Cosmochimica Acta* 388: 61–77. doi:10.1016/j.gca.2024.11.012

Anzures BA, Parman SW, Milliken RE, Namur O, Cartier C, Wang S (2020). Effect of sulfur speciation on chemical and physical properties of very reduced mercurian melts. *Geochimica et Cosmochimica Acta* 286: 1–18. doi:10.1016/j.gca.2020.07.024

Barros SCC, Demangeon ODS, Alibert Y, Leleu A, Adibekyan V, Lovis C, Bossini D, Sousa SG, Hara N, Bouchy F, Lavie B, Rodrigues J, da Silva JG, Lillo-Box J, Pepe FA, Tabernero HM, Osorio MRZ, Sozzetti A, Mascareño AS, Micela G, Prieto CA, Cristiani S, Damasso M, Di Marcantonio P, Ehrenreich D, Faria J, Figueira P, Hernández JIG, Jenkins J, Lo Curto G, Martins CJAP, Micela G, Nunes NJ, Pallé E, Santos NC, Rebolo R, Seager S, Twicken JD, Udry S, Vanderspek R, Winn JN (2022). HD

23472: a multi-planetary system with three super-Earths and two potential super-Mercuries. *Astronomy & Astrophysics* 665: A154. doi:10.1051/0004-6361/202244293

Benkhoff J, Murakami G, Baumjohann W, Besse S, Bunce E, Casale M, Cremosese G, Glassmeier KH, Hayakawa H, Heyner D, Hiesinger H, Huovelin J, Hussmann H, Iafolla V, Iess L, Kasaba Y, Kobayashi M, Milillo A, Mitrofanov IG, Montagnon E, Novara M, Orsini S, Quemerais E, Reininghaus U, Saito Y, Santoli F, Stramaccioni D, Sutherland O, Thomas N, Yoshikawa I, Zender J (2021). BepiColombo - Mission Overview and Science Goals. *Space Science Reviews* 217(8): 90. doi:10.1007/s11214-021-00861-4

Berthet S, Malavergne V, Righter K (2009). Melting of the Indarch meteorite (EH4 chondrite) at 1GPa and variable oxygen fugacity: Implications for early planetary differentiation processes. *Geochimica et Cosmochimica Acta* 73(20): 6402–6420. doi:10.1016/j.gca.2009.07.030

Bertone S, Mazarico E, Barker MK, Goossens S, Sabaka TJ, Neumann GA, Smith DE (2021). Deriving Mercury Geodetic Parameters With Altimetric Crossovers From the Mercury Laser Altimeter (MLA). *Journal of Geophysical Research: Planets* 126(4). doi:10.1029/2020je006683

Beuthe M, Charlier B, Namur O, Rivoldini A, Van Hoolst T (2020). Mercury's Crustal Thickness Correlates With Lateral Variations in Mantle Melt Production. *Geophysical Research Letters* 47(9). doi:10.1029/2020gl087261

Birch F (1947). Finite Elastic Strain of Cubic Crystals. *Physical Review* 71(11): 809–824. doi:10.1103/physrev.71.809

Blundy J, Wood B (2003). Partitioning of trace elements between crystals and melts. *Earth and Planetary Science Letters* 210(3-4): 383–397. doi:10.1016/s0012-821x(03)00129-8

Boujibar A, Habermann M, Righter K, Ross DK, Pando K, Righter M, Chidester BA, Danielson LR (2019). U, Th, and K partitioning between metal, silicate, and sulfide and implications for Mercury's structure, volatile content, and radioactive heat production. *American Mineralogist* 104(9): 1221–1237. doi:10.2138/am-2019-7000

Boujibar A, Righter K, Fontaine E, Collinet M, Lambart S, Nittler LR, Pando KM (2025). A Pyroxenite mantle on Mercury? Experimental insights from enstatite chondrite melting at pressures up to 5 GPa. *Icarus* 437: 116602. doi:10.1016/j.icarus.2025.116602

Boukaré C, Parman SW, Parmentier EM, Anzures BA (2019). Production and Preservation of Sulfide Layering in Mercury's Mantle. *Journal of Geophysical Research: Planets* 124(12): 3354–3372. doi:10.1029/2019je005942

Bowen NL (1914). The ternary system; diopside-forsterite-silica. *American Journal of Science* s4-38(225): 207–264. doi:10.2475/ajs.s4-38.225.207

Brown SM, Elkins-Tanton LT (2009). Compositions of Mercury's earliest crust from magma ocean models. *Earth and Planetary Science Letters* 286(3-4): 446–455. doi:10.1016/j.epsl.2009.07.010

Bunce EJ, Martindale A, Lindsay S, Muinonen K, Rothery DA, Pearson J, McDonnell I, Thomas C, Thornhill J, Tikkanen T, Feldman C, Huovelin J, Korpela S, Esko E, Lehtolainen A, Treis J, Majewski P, Hilchenbach M, Väisänen T, Luttinen A, Kohout T, Penttilä A, Bridges J, Joy KH, Alcacera-Gil MA, Alibert G, Anand M, Bannister N, Barcelo-Garcia C, Bicknell C, Blake O, Bland P, Butcher G, Cheney A, Christensen U, Crawford T, Crawford IA, Dennerl K, Dougherty M, Drumm P, Fairbend R, Genzer M, Grande M, Hall GP, Hodnett R, Houghton P, Imber S, Kallio E, Lara ML, Balado Margeli A, Mas-Hesse MJ, Maurice S, Milan S, Millington-Hotze P, Nenonen S, Nittler L, Okada T, Ormö J, Perez-Mercader J, Poyner R, Robert E, Ross D, Pajas-Sanz M, Schyns E, Seguy J, Strüder L, Vaudon N, Viceira-Martín J, Williams H, Willingale D, Yeoman T (2020). The BepiColombo Mercury Imaging X-Ray Spectrometer: Science Goals, Instrument Performance and Operations. *Space Science Reviews* 216(8): 126. doi:10.1007/s11214-020-00750-2

Byrne PK, Ostrach LR, Fassett CI, Chapman CR, Denevi BW, Evans AJ, Klimczak C, Banks ME, Head JW, Solomon SC (2016). Widespread effusive volcanism on Mercury likely ended by about 3.5 Ga. *Geophysical Research Letters* 43(14): 7408–7416. doi:10.1002/2016gl069412

Cartier C, Hammouda T, Doucelance R, Boyet M, Devidal JL, Moine B (2014). Experimental study of trace element partitioning between enstatite and melt in enstatite chondrites at low oxygen fugacities and 5 GPa. *Geochimica et Cosmochimica Acta* 130: 167–187. doi:10.1016/j.gca.2014.01.002

Cartier C, Namur O, Nittler L, Weider S, Crapster-Pregont E, Vorburger A, Frank E, Charlier B (2020). No FeS layer in Mercury? Evidence from Ti/Al measured by MESSENGER. *Earth and Planetary Science Letters* 534: 116108. doi:10.1016/j.epsl.2020.116108

Cartier C, Wood BJ (2019). The Role of Reducing Conditions in Building Mercury. *Elements* 15(1): 39–45. doi:10.2138/gselements.15.1.39

Chabot NL, Wollack EA, Klima RL, Minitti ME (2014). Experimental constraints on Mercury's core composition. *Earth and Planetary Science Letters* 390(0): 199–208. doi:10.1016/j.epsl.2014.01.004

Charlier B, Grove TL, Namur O, Holtz F (2018). Crystallization of the lunar magma ocean and the primordial mantle-crust differentiation of the Moon. *Geochimica et Cosmochimica Acta* 234: 50–69. doi:10.1016/j.gca.2018.05.006

Charlier B, Grove TL, Zuber MT (2013). Phase equilibria of ultramafic compositions on Mercury and the origin of the compositional dichotomy. *Earth and Planetary Science Letters* 363: 50–60. doi:10.1016/j.epsl.2012.12.021

Charlier B, Namur O (2019). The Origin and Differentiation of Planet Mercury. *Elements* 15(1): 9–14. doi:10.2138/gselements.15.1.9

Chen CH, Presnall D (1975). The system Mg2SiO4-SiO2 at pressures up to 25 kilobars. *American Mineralogist* 60(5-6_Part_1): 398–406

Cioria C, Mitri G, Connolly JAD, Perrillat J, Saracino F (2024). Mantle Mineralogy of Reduced Sub-Earths Exoplanets and Exo-Mercuries. *Journal of Geophysical Research: Planets* 129(7). doi:10.1029/2023je008234

Condamine P, Tournier S, Charlier B, Médard E, Triantafyllou A, Dalou C, Tissandier L, Lequin D, Cartier C, Füri E, Burnard PG, Demouchy S, Marrocchi Y (2022). Influence of intensive parameters and assemblies on friction evolution during piston-cylinder experiments. *American Mineralogist* 107(8): 1575–1581. doi:10.2138/am-2022-7958

Corgne A, Keshav S, Wood BJ, McDonough WF, Fei Y (2008). Metal–silicate partitioning and constraints on core composition and oxygen fugacity during Earth accretion. *Geochimica et Cosmochimica Acta* 72(2): 574–589. doi:10.1016/j.gca.2007.10.006

Cremonese G, Capaccioni F, Capria MT, Doressoundiram A, Palumbo P, Vincendon M, Massironi M, Debei S, Zusi M, Altieri F, Amoroso M, Aroldi G, Baroni M, Barucci A, Bellucci G, Benkhoff J, Besse S, Bettanini C, Blecka M, Borrelli D, Brucato JR, Carli C, Carlier V, Cerroni P, Cicchetti A, Colangeli L, Dami M, Da Deppo V, Della Corte V, De Sanctis MC, Erard S, Esposito F, Fantinel D, Ferranti L, Ferri F, Ficai Veltroni I, Filacchione G, Flamini E, Forlani G, Fornasier S, Forni O, Fulchignoni M, Galluzzi V, Gwinner K, Ip W, Jorda L, Langevin Y, Lara L, Leblanc F, Leyrat C, Li Y, Marchi S, Marinangeli L, Marzari F, Mazzotta Epifani E, Mendillo M, Mennella V, Mugnuolo R, Muinonen K, Naletto G, Noschese R, Palomba E, Paolinetti R, Perna D, Piccioni G, Politi R, Poulet F, Ragazzoni R, Re C, Rossi M, Rotundi A, Salemi G, Sgavetti M, Simioni E, Thomas N, Tommasi L, Turella A, Van Hoolst T, Wilson L, Zambon F, Aboudan A, Barraud O, Bott N, Borin P, Colombatti G, El Yazidi M, Ferrari S, Flahaut J, Giacomini L, Guzzetta L, Lucchetti A, Martellato E, Pajola M, Slemer A, Tognon G, Turrini D (2020). SIMBIO-SYS: Scientific Cameras and Spectrometer for the BepiColombo Mission. *Space Science Reviews* 216(5): 75. doi:10.1007/s11214-020-00704-8

Dickinson TL, McCoy TJ (1997). Experimental rare-earth-element partitioning in oldhamite: Implications for the igneous origin of aubritic oldhamite. *Meteoritics & Planetary Science* 32(3): 395–412. doi:10.1111/j.1945-5100.1997.tb01283.x

Elkins-Tanton LT (2012). Magma Oceans in the Inner Solar System. *Annual Review of Earth and Planetary Sciences* 40(1): 113–139. doi:10.1146/annurev-earth-042711-105503

Elkins-Tanton LT, Burgess S, Yin QZ (2011). The lunar magma ocean: Reconciling the solidification process with lunar petrology and geochronology. *Earth and Planetary Science Letters* 304(3-4): 326–336. doi:10.1016/j.epsl.2011.02.004

Elkins-Tanton LT, Parmentier EM, Hess PC (2003). Magma ocean fractional crystallization and cumulate overturn in terrestrial planets: Implications for Mars. *Meteoritics & Planetary Science* 38(12): 1753–1771. doi:10.1111/j.1945-5100.2003.tb00013.x

Falloon TJ, Green DH (1988). Anhydrous Partial Melting of Peridotite from 8 to 35 kb and the Petrogenesis of MORB. *Journal of Petrology* Special Volume(1): 379–414. doi:10.1093/petrology/special_volume.1.379

Fincham CJB, Richardson FD (1954). The behaviour of sulphur in silicate and aluminate melts. *Proceedings of the Royal Society of London A* 223(1152): 40–62. doi:10.1098/rspa.1954.0099

Fischer EL, Parman SW (2025). The bulk composition and initial size of Mercury. *Icarus* 439: 116664. doi:10.1016/j.icarus.2025.116664

Genova A, Goossens S, Mazarico E, Lemoine FG, Neumann GA, Kuang W, Sabaka TJ, Hauck SA, Smith DE, Solomon SC, Zuber MT (2019). Geodetic Evidence That Mercury Has A Solid Inner Core. *Geophysical Research Letters* 46(7): 3625–3633. doi:10.1029/2018gl081135

Goossens S, Renaud JP, Henning WG, Mazarico E, Bertone S, Genova A (2022). Evaluation of Recent Measurements of Mercury's Moments of Inertia and Tides Using a Comprehensive Markov Chain Monte Carlo Method. *The Planetary Science Journal* 3(2): 37. doi:10.3847/psj/ac4bb8

Gu T, Stagno V, Fei Y (2019). Partition coefficient of phosphorus between liquid metal and silicate melt with implications for the Martian magma ocean. *Physics of the Earth and Planetary Interiors* 295: 106298. doi:10.1016/j.pepi.2019.106298

Guillot B, Sator N (2007). A computer simulation study of natural silicate melts. Part I: Low pressure properties. *Geochimica et Cosmochimica Acta* 71(5): 1249–1265. doi:10.1016/j.gca.2006.11.015

Hart SR, Zindler A (1986). In search of a bulk-Earth composition. *Chemical Geology* 57(3-4): 247–267. doi:10.1016/0009-2541(86)90053-7

Hauck SA, Margot J, Solomon SC, Phillips RJ, Johnson CL, Lemoine FG, Mazarico E, McCoy TJ, Padovan S, Peale SJ, Perry ME, Smith DE, Zuber MT (2013). The curious case of Mercury's internal structure. *Journal of Geophysical Research: Planets* 118(6): 1204–1220. doi:10.1002/jgre.20091

Head JW, Chapman CR, Strom RG, Fassett CI, Denevi BW, Blewett DT, Ernst CM, Watters TR, Solomon SC, Murchie SL, Prockter LM, Chabot NL, Gillis-Davis JJ, Whitten JL, Goudge TA, Baker DMH, Hurwitz DM, Ostrach LR, Xiao Z, Merline WJ, Kerber L, Dickson JL, Oberst J, Byrne PK, Klimczak C, Nittler LR (2011). Flood Volcanism in the Northern High Latitudes of Mercury Revealed by MESSENGER. *Science* 333(6051): 1853–1856. doi:10.1126/science.1211997

Hiesinger H, J H, Alemanno G, Bauch K, D'Amore M, Maturilli A, Morlok A, Reitze M, Stangarone C, Stojic A, Varatharajan I, Weber I, the MERTIS Co-I Team (2020). Studying the Composition and Mineralogy of the Hermean Surface with the Mercury Radiometer and Thermal Infrared Spectrometer (MERTIS) for the BepiColombo Mission: An Update. *Space Science Reviews* 216(6): 110. doi:10.1007/s11214-020-00732-4

Ingrao N, Hammouda T, Boyet M, Gaborieau M, Moine B, Vlastelic I, Bouhifd M, Devidal JL, Mathon O, Testemale D, Hazemann JL, Proux O (2019). Rare earth element partitioning between sulphides and melt: Evidence for Yb2+ and Sm2+ in EH chondrites. *Geochimica et Cosmochimica Acta* 265: 182–197. doi:10.1016/j.gca.2019.08.036

Jarosewich E (1990). Chemical analyses of meteorites: A compilation of stony and iron meteorite analyses. *Meteoritics* 25(4): 323–337. doi:10.1111/j.1945-5100.1990.tb00717.x

Keil K (2010). Enstatite achondrite meteorites (aubrites) and the histories of their asteroidal parent bodies. *Geochemistry* 70(4): 295–317. doi:10.1016/j.chemer.2010.02.002

Kushiro I (1969). The System Forsterite Diopside-Silica With and Without Water at High Pressures. *American Journal of Science* 267-A: 269–294. doi:10.2475/001c.125224

Lange RA, Carmichael IS (1987). Densities of Na2O-K2O-CaO-MgO-FeO-Fe2O3-Al2O3-TiO2-SiO2 liquids: New measurements and derived partial molar properties. *Geochimica et Cosmochimica Acta* 51(11): 2931–2946. doi:10.1016/0016-7037(87)90368-1

Lark LH, Parman S, Huber C, Parmentier EM, Head JW (2022). Sulfides in Mercury's Mantle: Implications for Mercury's Interior as Interpreted From Moment of Inertia. *Geophysical Research Letters* 49(6): 2021 096713. doi:10.1029/2021gl096713

Lauretta DS, Goreva JS, Hill DH, Killgore M (2007). Bulk compositions of the CB chondrites Bencubbin, Fountain Hills, MAC 02675, and MIL 05082. *Lunar and Planetary Institute Conference Abstracts* 38: 2236. bibcode:2007LPI....38.2236L

Lesher CE, Spera FJ (2015). Thermodynamic and Transport Properties of Silicate Melts and Magma. In Sigurdsson H (ed.) *The Encyclopedia of Volcanoes*, p. 113–141. Elsevier. doi:10.1016/b978-0-12-385938-9.00005-5

Ma C, Beckett JR, Rossman GR (2011). Murchisite, Cr5S6, a new mineral from the Murchison meteorite. *American Mineralogist* 96(11-12): 1905–1908. doi:10.2138/am.2011.3858

Ma Z (2001). Thermodynamic description for concentrated metallic solutions using interaction parameters. *Metallurgical and Materials Transactions B* 32(1): 87–103. doi:10.1007/s11663-001-0011-0

Malavergne V, Toplis MJ, Berthet S, Jones J (2010). Highly reducing conditions during core formation on Mercury: Implications for internal structure and the origin of a magnetic field. *Icarus* 206(1): 199–209. doi:10.1016/j.icarus.2009.09.001

Margot J, Peale SJ, Solomon SC, Hauck SA, Ghigo FD, Jurgens RF, Yseboodt M, Giorgini JD, Padovan S, Campbell DB (2012). Mercury's moment of inertia from spin and gravity data. *Journal of Geophysical Research: Planets* 117(E12). doi:10.1029/2012je004161

McCoy TJ, Dickinson TL, Lofgren GE (1999). Partial melting of the Indarch (EH4) meteorite: A textural, chemical, and phase relations view of melting and melt migration. *Meteoritics & Planetary Science* 34(5): 735–746. doi:10.1111/j.1945-5100.1999.tb01386.x

McCoy TJ, Peplowski PN, McCubbin FM, Weider SZ (2018). The Geochemical and Mineralogical Diversity of Mercury. In Solomon S, Nittler L, Anderson B (eds.) *Mercury*, p. 176–190. Cambridge University Press. doi:10.1017/9781316650684.008

McCubbin FM, Riner MA, Vander Kaaden KE, Burkemper LK (2012). Is Mercury a volatile-rich planet? *Geophysical Research Letters* 39(9): 09202. doi:10.1029/2012gl051711

McDonough WF (2025). Earth's composition: Origin, energy budget, and insights from geoneutrinos. *Geochimica et Cosmochimica Acta* doi:10.1016/j.gca.2025.12.060

Mitrofanov IG, Kozyrev AS, Lisov DI, Litvak ML, Malakhov AA, Mokrousov MI, Benkhoff J, Owens A, Schulz R, Quarati F (2021). The Mercury Gamma-Ray and Neutron Spectrometer (MGNS) Onboard the Mercury Planetary Orbiter of the BepiColombo Mission: Design Updates and First Measurements in Space. *Space Science Reviews* 217(5): 67. doi:10.1007/s11214-021-00842-7

Morgan JW, Anders E (1980). Chemical composition of Earth, Venus, and Mercury. *Proceedings of the National Academy of Sciences* 77(12): 6973–6977. doi:10.1073/pnas.77.12.6973

Mouser MD, Dygert N (2023). On the Potential for Cumulate Mantle Overturn in Mercury. *Journal of Geophysical Research: Planets* 128(7). doi:10.1029/2023je007739

Mouser MD, Dygert N, Anzures BA, Grambling NL, Hrubiak R, Kono Y, Shen G, Parman SW (2021). Experimental Investigation of Mercury's Magma Ocean Viscosity: Implications for the Formation of Mercury's Cumulate Mantle, Its Subsequent Dynamic Evolution, and Crustal Petrogenesis. *Journal of Geophysical Research: Planets* 126(11). doi:10.1029/2021je006946

Murrell M, Burnett D (1982). Actinide microdistributions in the enstatite meteorites. *Geochimica et Cosmochimica Acta* 46(12): 2453–2460. doi:10.1016/0016-7037(82)90368-4

Mysen BO (1983). The structure of silicate melts. *Annual Review of Earth and Planetary Sciences* 11(1): 75–97. doi:10.1146/annurev.ea.11.050183.000451

Namur O, Charlier B (2017). Silicate mineralogy at the surface of Mercury. *Nature Geoscience* 10(1): 9–13. doi:10.1038/ngeo2860

Namur O, Charlier B, Holness MB (2012). Dual origin of Fe–Ti–P gabbros by immiscibility and fractional crystallization of evolved tholeiitic basalts in the Sept Iles layered intrusion. *Lithos* 154: 100–114. doi:10.1016/j.lithos.2012.06.034

Namur O, Charlier B, Holtz F, Cartier C, McCammon C (2016a). Sulfur solubility in reduced mafic silicate melts: Implications for the speciation and distribution of sulfur on Mercury. *Earth and Planetary Science Letters* 448: 102–114. doi:10.1016/j.epsl.2016.05.024

Namur O, Collinet M, Charlier B, Grove TL, Holtz F, McCammon C (2016b). Melting processes and mantle sources of lavas on Mercury. *Earth and Planetary Science Letters* 439: 117–128. doi:10.1016/j.epsl.2016.01.030

Nittler LR, Boujibar A, Crapster-Pregont E, Frank EA, McCoy TJ, McCubbin FM, Starr RD, Vorburger A, Weider SZ (2023). Chromium on Mercury: New Results From the MESSENGER X-Ray Spectrometer and Implications for the Innermost Planet's Geochemical Evolution. *Journal of Geophysical Research: Planets* 128(7). doi:10.1029/2022je007691

Nittler LR, Chabot NL, Grove TL, Peplowski PN (2018). The Chemical Composition of Mercury. In Solomon S, Nittler L, Anderson B (eds.) *Mercury*, p. 30–51. Cambridge University Press. doi:10.1017/9781316650684.003

Nittler LR, Frank EA, Weider SZ, Crapster-Pregont E, Vorburger A, Starr RD, Solomon SC (2020). Global major-element maps of Mercury from four years of MESSENGER X-Ray Spectrometer observations. *Icarus* 345: 113716. doi:10.1016/j.icarus.2020.113716

Nittler LR, Starr RD, Weider SZ, McCoy TJ, Boynton WV, Ebel DS, Ernst CM, Evans LG, Goldsten JO, Hamara DK, Lawrence DJ, McNutt RL, Schlemm CE, Solomon SC, Sprague AL (2011). The Major-Element Composition of Mercury's Surface from MESSENGER X-ray Spectrometry. *Science* 333(6051): 1847–1850. doi:10.1126/science.1211567

Ohtani E, Maeda M (2001). Density of basaltic melt at high pressure and stability of the melt at the base of the lower mantle. *Earth and Planetary Science Letters* 193(1-2): 69–75. doi:10.1016/s0012-821x(01)00505-2

O'Neill HS (2021). The Thermodynamic Controls on Sulfide Saturation in Silicate Melts with Application to Ocean Floor Basalts. In Moretti R, Neuville D (eds.) *Magma redox geochemistry*, p. 177–213. Wiley. doi:10.1002/9781119473206.ch10

Padovan S, Wieczorek MA, Margot J, Tosi N, Solomon SC (2015). Thickness of the crust of Mercury from geoid-to-topography ratios. *Geophysical Research Letters* 42(4): 1029–1038. doi:10.1002/2014gl062487

Peplowski PN, Evans LG, Hauck SA, McCoy TJ, Boynton WV, Gillis-Davis JJ, Ebel DS, Goldsten JO, Hamara DK, Lawrence DJ, McNutt RL, Nittler LR, Solomon SC, Rhodes EA, Sprague AL, Starr RD, Stockstill-Cahill KR (2011). Radioactive Elements on Mercury's Surface from MESSENGER: Implications for the Planet's Formation and Evolution. *Science* 333(6051): 1850–1852. doi:10.1126/science.1211576

Pirotte H, Cartier C, Namur O, Pommier A, Zhang Y, Berndt J, Klemme S, Charlier B (2023). Internal differentiation and volatile budget of Mercury inferred from the partitioning of heat-producing elements at highly reduced conditions. *Icarus* 405: 115699. doi:10.1016/j.icarus.2023.115699

Pitsch S, Connolly JAD, Schmidt MW, Sossi PA, Liebske C (2025). Solids and liquids in the (Fe, Mg, Ca)S-system: experimentally determined and thermodynamically modelled phase relations. *Physics and Chemistry of Minerals* 52(2): 12. doi:10.1007/s00269-025-01313-z

Pommier A, Tauber M, Pirotte H, Cody G, Steele A, Bullock E, Charlier B, Mysen B (2023). Experimental investigation of the bonding of sulfur in highly reduced silicate glasses and melts. *Geochimica et Cosmochimica Acta* 363: 114–128. doi:10.1016/j.gca.2023.10.027

Presnall DC (1995). Phase Diagrams of Earth-Forming Minerals. In Ahrens T (ed.) *Mineral physics & crystallography: a handbook of physical constants*, p. 248–268. American Geophysical Union. doi:10.1029/rf002p0248

Riel N, Kaus BJP, Green ECR, Berlie N (2022). MAGEMin, an Efficient Gibbs Energy Minimizer: Application to Igneous Systems. *Geochemistry, Geophysics, Geosystems* 23(7). doi:10.1029/2022gc010427

Riner MA, Bina CR, Robinson MS, Desch SJ (2008). Internal structure of Mercury: Implications of a molten core. *Journal of Geophysical Research: Planets* 113(E8). doi:10.1029/2007je002993

Rothery DA, Massironi M, Alemanno G, Barraud O, Besse S, Bott N, Brunetto R, Bunce E, Byrne P, Capaccioni F, Capria MT, Carli C, Charlier B, Cornet T, Cremonese G, D'Amore M, De Sanctis MC, Doressoundiram A, Ferranti L, Filacchione G, Galluzzi V, Giacomini L, Grande M, Guzzetta LG, Helbert J, Heyner D, Hiesinger H, Hussmann H, Hyodo R, Kohout T, Kozyrev A, Litvak M, Lucchetti A, Malakhov A, Malliband C, Mancinelli P, Martikainen J, Martindale A, Maturilli A, Milillo A, Mitrofanov I, Mokrousov M, Morlok A, Muinonen K, Namur O, Owens A, Nittler LR, Oliveira JS, Palumbo P, Pajola M, Pegg DL, Penttilä A, Politi R, Quarati F, Re C, Sanin A, Schulz R, Stangarone C, Stojic A, Tretiyakov V, Väisänen T, Varatharajan I, Weber I, Wright J, Wurz P, Zambon F (2020). Rationale for BepiColombo Studies of Mercury's Surface and Composition. *Space Science Reviews* 216(4): 66. doi:10.1007/s11214-020-00694-7

Santerne A, Brugger B, Armstrong DJ, Adibekyan V, Lillo-Box J, Gosselin H, Aguichine A, Almenara JM, Barrado D, Barros SCC, Bayliss D, Boisse I, Bonomo AS, Bouchy F, Brown DJA, Deleuil M, Delgado Mena E, Demangeon O, Díaz RF, Doyle A, Dumusque X, Faedi F, Faria JP, Figueira P, Foxell E, Giles H, Hébrard G, Hojjatpanah S, Hobson M, Jackman J, King G, Kirk J, Lam KWF, Ligi R, Lovis C, Louden T, McCormac J, Mousis O, Neal JJ, Osborn HP, Pepe F, Pollacco D, Santos NC, Sousa SG, Udry S, Vigan A (2018). An Earth-sized exoplanet with a Mercury-like composition. *Nature Astronomy* 2(5): 393–400. doi:10.1038/s41550-018-0420-5

Saracino F, Charlier B, Zhang Y, Lécaille M, Lin Y, Namur O (2025). The role of sulfur on the liquidus temperature and olivine-orthopyroxene equilibria in highly reduced magmas. *Chemical Geology* 683: 122777. doi:10.1016/j.chemgeo.2025.122777

Saracino F, Charlier B, Zhang Y, Namur O (2026). Chemical analyses of experimental products and magma ocean crystallization model for Mercury. Version v10. Zenodo. doi:10.5281/zenodo.20273496

Schaefer L, Elkins-Tanton LT (2018). Magma oceans as a critical stage in the tectonic development of rocky planets. *Philosophical Transaction of the Royal Society A* 376(2132): 20180109. doi:10.1098/rsta.2018.0109

Schmidt MW, Kraettli G (2022). Experimental Crystallization of the Lunar Magma Ocean, Initial Selenotherm and Density Stratification, and Implications for Crust Formation, Overturn and the Bulk Silicate Moon Composition. *Journal of Geophysical Research: Planets* 127(5): 5. doi:10.1029/2022je007187

Schubert G, Ross M, Stevenson D, Spohn T (1988). Mercury's thermal history and the generation of its magnetic field. In Vilas F, Chapman C, Matthews M (eds.) *Mercury*, p. 429–460. University of Arizona Press. doi:10.2307/j.ctv1v090nx.17

Smith DE, Zuber MT, Phillips RJ, Solomon SC, Hauck SA, Lemoine FG, Mazarico E, Neumann GA, Peale SJ, Margot JL, Johnson CL, Torrence MH, Perry ME, Rowlands DD, Goossens S, Head JW, Taylor AH (2012). Gravity Field and Internal Structure of Mercury from MESSENGER. *Science* 336(6078): 214–217. doi:10.1126/science.1218809

Snyder GA, Taylor LA, Neal CR (1992). A chemical model for generating the sources of mare basalts: Combined equilibrium and fractional crystallization of the lunar magmasphere. *Geochimica et Cosmochimica Acta* 56(10): 3809–3823. doi:10.1016/0016-7037(92)90172-f

Solomatov V (2015). Magma Oceans and Primordial Mantle Differentiation. In Schubert G (ed.) *Treatise on Geophysics*, vol. 9, p. 81–104. Elsevier. doi:10.1016/b978-0-444-53802-4.00155-x

Steenstra E, Seegers A, Putter R, Berndt J, Klemme S, Matveev S, Bullock E, van Westrenen W (2020a). Metal-silicate partitioning systematics of siderophile elements at reducing conditions: A new experimental database. *Icarus* 335: 113391. doi:10.1016/j.icarus.2019.113391

Steenstra E, Trautner V, Berndt J, Klemme S, van Westrenen W (2020b). Trace element partitioning between sulfide-, metal- and silicate melts at highly reduced conditions: Insights into the distribution of volatile elements during core formation in reduced bodies. *Icarus* 335: 113408. doi:10.1016/j.icarus.2019.113408

Steinbrügge G, Dumberry M, Rivoldini A, Schubert G, Cao H, Schroeder DM, Soderlund KM (2021). Challenges on Mercury's Interior Structure Posed by the New Measurements of its Obliquity and Tides. *Geophysical Research Letters* 48(3). doi:10.1029/2020gl089895

Vander Kaaden KE, McCubbin FM (2015). Exotic crust formation on Mercury: Consequences of a shallow, FeO-poor mantle. *Journal of Geophysical Research: Planets* 120(2): 195–209. doi:10.1002/2014je004733

Walker D, Longhi J, Hays JF (1975). Differentiation of a very thick magma body and implications for the source region of mare basalts. *Proceedings of the Lunar Science Conference* 6: 1103–1120. bibcode:1975LPSC....6.1103W

Walter MJ, Presnall DC (1994). Melting Behavior of Simplified Lherzolite in the System CaO-MgO-Al2O3-SiO2-Na2O from 7 to 35 kbar. *Journal of Petrology* 35(2): 329–359. doi:10.1093/petrology/35.2.329

Wang Y, Xiao Z, Xu R (2022). Multiple Mantle Sources of High-Magnesium Terranes on Mercury. *Journal of Geophysical Research: Planets* 127(5). doi:10.1029/2022je007218

Warren PH (1988). The origin of pristine KREEP: effects of mixing between UrKREEP and the magmas parental to the Mg-rich cumulates. In *Lunar and Planetary Science Conference Proceedings 233–241*. bibcode:1988LPSC...18..233W

Warren PH, Wasson JT (1979). The origin of KREEP. *Reviews of Geophysics* 17(1): 73–88. doi:10.1029/rg017i001p00073

Weider SZ, Nittler LR, Starr RD, Crapster-Pregont EJ, Peplowski PN, Denevi BW, Head JW, Byrne PK, Hauck SA, Ebel DS, Solomon SC (2015). Evidence for geochemical terranes on Mercury: Global mapping of major elements with MESSENGER's X-Ray Spectrometer. *Earth and Planetary Science Letters* 416: 109–120. doi:10.1016/j.epsl.2015.01.023

Weisberg MK, Prinz M, Clayton RN, Mayeda TK, Sugiura N, Zashu S, Ebihara M (2001). A new metal-rich chondrite grouplet. *Meteoritics & Planetary Science* 36(3): 401–418. doi:10.1111/j.1945-5100.2001.tb01882.x

Weisberg MK, Prinz M, Humayun M, Campbell AJ (2000). Origin of metal in the CB (Bencubbinite) chondrites. *Lunar and Planetary Institute Conference Abstracts* 31: 1466. bibcode:2000LPI....31.1466W

Weng YH, Presnall DC (2001). The system diopside forsterite enstatite at 5.1 GPa: a ternary model for melting of the mantle. *The Canadian Mineralogist* 39(2): 299–308. doi:10.2113/gscanmin.39.2.299

White WM (2020). *Geochemistry*. Wiley-Blackwell, 2nd edn.

Wilbur ZE, Udry A, McCubbin FM, vander Kaaden KE, DeFelice C, Ziegler K, Ross DK, McCoy TJ, Gross J, Barnes JJ, Dygert N, Zeigler RA, Turrin BD, McCoy C (2022). The effects of highly reduced magmatism revealed through aubrites. *Meteoritics & Planetary Science* 57(7): 1387–1420. doi:10.1111/maps.13823

Wohlers A, Wood BJ (2017). Uranium, thorium and REE partitioning into sulfide liquids: Implications for reduced S-rich bodies. *Geochimica et Cosmochimica Acta* 205: 226–244. doi:10.1016/j.gca.2017.01.050

Xu Y, Lin Y, Wu P, Namur O, Zhang Y, Charlier B (2024). A diamond-bearing core-mantle boundary on Mercury. *Nature Communications* 15(1): 5061. doi:10.1038/s41467-024-49305-x

Zhang Y, Charlier B, Krein SB, Grove TL, Namur O, Holtz F (2024). The very late-stage crystallization of the lunar magma ocean and the composition of immiscible urKREEP. *Earth and Planetary Science Letters* 646: 118989. doi:10.1016/j.epsl.2024.118989

Zolotov MY, Sprague AL, Hauck SA, Nittler LR, Solomon SC, Weider SZ (2013). The redox state, FeO content, and origin of sulfur-rich magmas on Mercury. *Journal of Geophysical Research: Planets* 118(1): 138–146. doi:10.1029/2012je004274